This is a preprint, the final version is subject to change, of the American Mineralogist (MSA)
Cite as Authors (Year) Title. American Mineralogist, in press.
DOI: https://doi.org/10.2138/am-2020-7326

Revision 1

Systematics of H_2 and H_2O evolved from chlorites during oxidative dehydrogenation

Małgorzata Lempart (1) *, Arkadiusz Derkowski (1) *, Tomasz Strączek (2), Czesław Kapusta (2)

(1) Institute of Geological Sciences, Polish Academy of Sciences, Research Centre in Krakow, Senacka St. No. 1, PL-31002 Krakow, Poland (2) AGH University of Science and Technology, Faculty of Physics and Applied Computer Sciences, Al. Mickiewicza St. No. 30, PL-30059, Krakow, Poland

* Corresponding authors email: ndlempar@cyf-kr.edu.pl (M. Lempart); ndderkow@cyf-kr.edu.pl (A. Derkowski)

Abstract

Thermally-induced dehydroxylation and oxidative dehydrogenation drive the thermal decomposition of all Fe(II)-containing phyllosilicates. Whereas the former produces H_2O gas, the latter results in H_2 evolution. Six chlorites representing the Mg-Fe(II) series from clinochlore to chamosite and biotite (as an analogue of the 2:1 layer in chlorite) were investigated using thermogravimetry coupled to quadrupole mass spectroscopy (TG-MS). A fast-ramp heating protocol was applied to identify if and how hydrogen gas was released from the crystal structure and whether it was quantitatively related to structural Fe(II) content. Dehydroxylation and oxidative dehydrogenation were tested under inert and oxidizing conditions.

H_2 liberation, shown by an evolution of the m/z=2 signal for chamosites, Fe-rich clinochlores, and biotite heated under nitrogen gas atmosphere, confirmed the H_2 gas production by oxidative dehydrogenation. Along with H_2 evolution, H_2O (m/z=18) was released, suggesting that dehydroxylation is a trigger for dehydrogenation. The higher the Fe(II) content in the studied chlorites, the more intense the H_2 evolution, thus the higher the H_2/H_2O ratios. The products of ramp-heating to 1000 °C resulted in varying amounts of newly-formed Fe(III) (from 7 to 22 %), however, biotite that converted into oxybiotite underwent almost complete oxidation, indicating a stronger tendency of 2:1 layer to dehydrogenation. The observed concurrent, but independent mechanisms of H_2 and H_2O evolution produced a feasible model of the thermal decomposition of chlorites.

Despite O_2 availability under oxidizing condition, the Fe(II) oxidation was not driven by attaching oxygen anions to the phyllosilicate structure, but also by dehydrogenation. Hydrogen was not detected using MS for any tested sample heated in synthetic air because any H_2, if released, was instantaneously combined with external O_2, which resulted in an

excess H_2O MS signal not matched by mass loss on the TG profiles of chamosite and biotite. Without coupling of the evolved gas analysis with TG, the excess H_2O produced by dehydrogenation in the O_2-bearing carrier gas would result in misleading interpretations of dehydroxylation.

Methodological and geological implications of the TG-MS experiments are discussed. The oxidation of Fe(II) in all Fe(II)-containing phyllosilicates proceeds with simultaneous H_2 gas release that is not dependent on oxygen fugacity nor temperature during the mineral formation. Therefore, the correlation between Fe^{3+}/Fe^{2+} and remaining hydrogen in the structure must be considered during modeling the conditions that involve chlorite as geothermobarometer. H_2 release during heating is proposed as an indicator for oxidative dehydrogenation of Fe(II)-bearing minerals on Mars.

Keywords: chlorite, hydrogen, evolved gas analysis, dehydrogenation, dehydroxylation, oxidation.

Introduction

Interest in chlorites stems from their abundance in various geological environments, their complex layering, and high content of OH groups. Chlorites form mainly in low- to intermediate-grade metamorphic mafic and ultramafic rocks, and in sedimentary rocks (Deer et al. 1992). They commonly occur in the Earth's crust, as well as, on Mars (Mustard et al. 2008), where their presence enables identification of hydrothermal and/or low-grade metamorphic formation conditions (Ehlmann et al. 2011). Water released from chlorites under specific temperature and pressure conditions strongly affects melting, crystallization, and transport processes in the lithosphere. Indeed, chlorite is one of the main hydrous phases ("structural water" content ~13 wt%) in peridotite, basalt, and sediment components of the slab that releases fluids participating in the rehydration of the mantle wedge (Goto and Tatsumi 1990; Grove et al. 2012).

The high structural water content in chlorites results from a structure comprised of two hydroxyl-rich layers: the octahedral sheet sandwiched between two tetrahedral sheets (2:1 layer) and compensating for the negative tetrahedral charge the octahedral hydroxide sheet in the interlayer (Foster 1962; Wiewióra and Weiss 1990). Tri-, trioctahedral species of the series represented by clinochlore and chamosite are the types of chlorite most common in nature. Along with other phyllosilicates, chlorites undergo dehydroxylation when heated, which results in the formation and release of H_2O:

$$(OH)_{2n} \rightarrow nH_2O + nO_r \quad (1)$$

The newly formed water molecules migrate through the lattice of the phyllosilicate leaving the residual oxygen (O_r) in the structure (Drits et al. 1995). Theoretically, due to much weaker OH bonding and the proximity of OH groups, the interlayer octahedral sheet should undergo dehydroxylation at a lower temperature than the octahedral sheet in the 2:1 layer (Brett et al.

1970), resulting in two discrete mass loss events (Steudel et al. 2016): a first event of interlayer dehydroxylation:

$$[(R^{2+}R^{3+})_3(OH)_6][(Si_3Al)R_3^{2+}O_{10}(OH)_2] \rightarrow [(R^{2+}R^{3+})_3(O_r)_3][(Si_3Al)R_3^{2+}O_{10}(OH)_2] + 3H_2O\uparrow \quad (2a)$$

and a second event of dehydroxylation in the 2:1 layer:

$$[(R^{2+}R^{3+})_3(O_r)_3][(Si_3Al)R_3^{2+}O_{10}(OH)_2] \rightarrow [(R^{2+}R^{3+})_3(O_r)_3][(Si_3Al)R_3^{2+}O_{10}O_r] + H_2O\uparrow, \quad (2b)$$

where R^{2+} equals Mg^{2+}, Fe^{2+}, and Mn^{2+} and R^{3+} for Fe^{3+} and Cr^{3+}. Because there is a different number of hydroxyl groups involved in the above reactions, the recorded mass loss ratio is expected to be 3:1. However, in Fe(II)-containing chlorite, the content of OH groups, and the quantity of "structural water" potentially released during heating, is decreased by dehydrogenation occurring prior to, or simultaneously with dehydroxylation (Lempart et al. 2018).

Dehydrogenation proceeds in a vacuum and in an inert gas atmosphere during thermal decomposition of all Fe(II)-containing phyllosilicates, causing the removal of one hydrogen atom, while oxidizing one Fe(II) cation that is octahedrally coordinated with the OH group (Farmer et al. 1971; MacKenzie and Berezowski 1981; Sanz et al. 1983; Rancourt et al. 2001):

$$Fe^{2+} + OH^- \rightarrow Fe^{3+} + O_r^{2-} + \tfrac{1}{2}\, H_2\uparrow. \quad (3)$$

Dehydrogenation changes the expected 3:1 mass loss ratio proportionally to Fe(II) content in the two octahedral-chlorite sheets (Steudel et al. 2016; Lempart et al. 2018). Certain heating regimes can enhance dehydrogenation over dehydroxylation; the extent of Fe(II) oxidation and mineralogical products of structural alteration depend strongly on the heating pattern (rate and temperature; Lempart et al. 2018).

Under inert gas dehydroxylation and accompanying dehydrogenation should result in the evolution H_2O and H_2 gas, respectively. Under oxidizing atmosphere dehydrogenation

may also occur, however without H_2 gas production because the evolving hydrogen should immediately react with an external oxygen present on the crystal surface, forming a water molecule. For a reaction under O_2-bearing atmosphere MacKenzie and Berezowski (1981, 1984) presented the Equation 3 in the following manner:

$$4(Fe^{2+} + OH^-) + O_2 \rightarrow 4(Fe^{3+} + O_r^{2-}) + 2H_2O\uparrow. \quad (4)$$

Although O_2 gas enhances dehydrogenation and Fe(II) oxidation, the mechanism responsible for the two reactions described by Equations 3 and 4 seems to proceed independently of ambient gas type (Lempart et al. 2018). Moreover, when a mineral structure does not contain Fe(II)-linked to hydroxyl hydrogen, instead of oxidative dehydrogenation following Equation 4 the Fe(II) oxidation proceeds by binding oxygen (Addison and Sharp 1962):

$$4Fe^{2+} + O_2 \rightarrow 4Fe^{3+} + 2O_r^{2-} \quad (5)$$

and results in mass gain.

If Equation 3 holds true, H_2 should be measured as volatile during heating, and quantitatively correspond to the extent of Fe(II) oxidation. However, only a few studies noted the release of hydrogen during heating of Fe(II)-containing phyllosilicates (Rouxhet et al. 1972; Norman and Palin 1982; MacKenzie et al. 1986; Villiéras et al. 1992; Steudel et al. 2016). Moreover, no correlation between thermally evolved H_2 and Fe(II) content in phyllosilicates has been observed (Heller-Kallai et al. 1989; Heller-Kallai 1997; Heide and Földvari 2006). Norman and Palin (1982) noted some H_2 liberation during heating of chlorite, biotite, and muscovite. Similarly, Charsley et al. (1987) observed H_2 released from chamosite heated under a nitrogen gas atmosphere. However, these studies did not link H_2 release with dehydrogenation following Equation 3, instead it was explained by the reduction of evolved water to hydrogen on exposed Fe(II) or a breakdown of Fe-OH and Al-OH bonds forming the

H_2 gas instead of H_2O. Steudel et al. (2016) associated H_2 release from chlorite to Fe(II) oxidation reaction; however, methodological issues made further interpretation difficult.

Among OH-rich phyllosilicates, the clinochlore-chamosite series is a unique, structurally uniform Mg-Fe(II) solid solution, common in nature, with available specimens of almost any Fe(II)/Mg ratio. In addition, chlorites dehydroxylate entirely at temperatures below 900 °C, which is lower than trioctahedral micas, making them methodologically suitable for numerous thermal experiments (Vedder and Wilkins 1969; Brett et al. 1970). For these reasons, Mg-Fe(II) series of chlorite was chosen to test for H_2 evolution during heating. The 2:1 layer in chlorite is analogous to vermiculite and mica, therefore, a biotite sample was also used in a thermally-induced dehydrogenation test as a reference material (Sanz et al. 1983; Rancourt et al. 1993).

The overall aim of the study, which follows the paper by Lempart et al. (2018), was to determine whether dehydrogenation produces H_2 gas quantitatively and separately from dehydroxylation, and corresponds to Fe(II) oxidation. This aim was accomplished through testing the validity of Equations 3 and 4 for the selected series of six tri-, trioctahedral Mg-Fe chlorites and biotite using thermogravimetry coupled with evolved gas analysis and ex-situ analyses of the reaction end-products.

Samples and sample characterization methods

Six tri-, trioctahedral chlorites were selected for study as chemically and structurally pure samples. The chemical compositions were obtained via microprobe analyses and Mössbauer spectroscopy (Supplemental Table S1) (methodology described by Lempart et al. 2018 and Luberda-Durnaś et al. 2019). LP-6 biotite as a pure and homogenous reference material commonly used in K-Ar geochronology (Ingamells and Engels 1976) was used as a

reference for the tri-, trioctahedral chlorite 2:1 layer. All relevant characterization of the studied samples was summarized in Table 1.

Based on the X-ray diffraction (XRD) study of Luberda-Durnaś et al. (2019), these samples are nearly pure trioctahedral IIb-even (IIbb) chlorites. The Mal, Sptb, MtBl and SG7 samples have <3% quartz and there is rutile in POST. Interstratifications with 7Å phases or their admixture were excluded, whereas minor interstratification by different polytypes is possible. Evolved gas analysis revealed minor SO_2 evolution that may originate from pyrite impurities in SG7, and a minor CO_2 peak in SG7, Mal, POST, and LP-6 from trace carbonate minerals, all not detectable by XRD.

Mössbauer spectroscopy was used to quantify the relative proportions of Fe(II) and Fe(III) in the natural samples and after heating to 1000 °C (Taylor et al. 1968). ^{57}Fe Mössbauer measurements were performed at room temperature (300K) in transmission mode using a MOSIEK 3E constant acceleration spectrometer (manufactured by "Elektronika Jądrowa", Kraków), featuring a proportional Xe gas detector and band pass filter set for the 14.4 keV line. A 20 mCi source of ^{57}Co in a Rhodium matrix was used. A powdered sample of each material was placed in a bag made of PELD foil and lightly pressed to form a thin pellet of 3 mm in diameter to avoid any saturation effect, and thus provided an isotropic distribution of the electric field gradient. The thickness was adjusted to obtain a 3-fold attenuation of the incident beam. The time of one measurement was 160 hours. Fitting was performed using Gauss-Newton's iterative method of minimizing $\chi 2$ (Chrisman and Tumolillo 1971), with the shape of the spectrum calculated using the transmission integral method. The relative ratio of the recoil-free fraction (f) of Fe(III) and Fe(II) (f^{3+}/f^{2+}) was assumed to be approximately 1.00 for natural chlorites (Kodama et al. 1982; Aja and Dyar 2002), 1.28 for natural and heated biotite (Dyar et al. 2008) and ~1.22 for thermal reaction products of

chlorite (De Grave and Van Alboom 1991) (see detailed discussion in Supplemental Information).

Experimental procedures

Thermogravimetric (TG) experiments were performed using a TA Discovery instrument (TA Instruments, USA) with a weighing error of <1 μg, weight measurement accuracy of <0.1 μg, and a thermal drift between 200 °C and 1000 °C of <4 μg. To detect gases evolving from samples during heating, gas outlet of the TG instrument was coupled with a ThermoStar^{TM}, GDS 320 quadrupole mass spectrometer (MS) (Pfeiffer Vacuum, Germany) with an electron ionization energy of 70 eV. Twenty mg of air-dried powder sample were loaded into a Pt crucible and dried in a TG furnace, isothermally, for 1 hour at 200 °C to remove adsorbed water, then heated to 1000 °C at a 20°C/min rate in dry nitrogen gas (>99.999% purity) or synthetic air (>99.99% purity) with a flow rate of 100 cm^3/min. Biotite was heated to 1050 °C due to a higher temperature of decomposition (Vedder and Wilkins 1969). Just before starting the TG experiments in dry nitrogen gas, the TG furnace and balance were purged with nitrogen gas at a 100–200 cm^3/min rate. To ensure the absence of residual O_2 gas in the TG furnace atmosphere, CuC_2O_4 (standard reference material, TA Instruments) was analyzed before conducting the experiments. TG experiments were run twice to check reproducibility; a mean total weight loss' standard deviation of 0.05 wt% was found for ramp heating measurements. The total mass loss (Δm_{dx}) during all TG experiments was calculated as the difference between the mass at 205 °C (end of drying step) and the minimum mass determined near 1000 °C. In contrast to the long-term isothermal heating experiments of Lempart et al. (2018) where dehydrogenation was strongly enhanced by isothermal heating, in the present study the fast ramp heating procedure was required to obtain a portion of the evolved gas, measurable quantitatively using MS as a function of heating time

and temperature. For the MtBl sample, however, isothermal heating at 400 °C for 48 hours followed by ramp heating to 1000 °C at a rate of 20°C/min was also performed.

The composition of the evolved gas and changes in sample weight were determined simultaneously with TG experiments. To prevent vapor condensation, a quartz glass capillary was heated to 200 °C, while the gas inlet was kept at 120 °C. In MS recording, the intensities (current) of the selected ions were monitored: H_2O^+ m/z = 18, H_2^+ m/z = 2, CO_2^+ m/z = 44, SO_2^+ m/z = 64, O_2 m/z = 32, and H_2S^+ m/z = 34. In addition, the selected daughter ions such as H^+ m/z = 1, O^+ m/z = 16, OH^+ m/z = 17, C^+ m/z = 12, and CO^+ m/z = 28 (above baseline in N_2 carrier gas) were monitored to check any fragmentation of the above-listed molecule ions. Monitoring of daughter ion intensities was essential to exclude the evolution of hydrogen coming from H_2O fragmentation. The MS dwell time was 200 ms, in which selected m/z ion signals were collected, hence 1 scan per 2 s was collected for the previously listed masses. The maximum delay time between tested ion current masses was 1s (between m/z = 18 and m/z = 64), which corresponded to only a 0.3 °C temperature shift. The TG system background contributions were periodically verified via blank (empty TG pan) runs between sample measurements. The obtained mass spectra are shown without background correction.

The quantitative contribution of DTG curve (the first derivative of TG curve over time) and MS spectra (the ion current corresponding to H_2O^+ or H_2^+) was determined by integrating the corresponding peak areas. The boundary between different thermal events was determined at the minimum of the DTG curve and/or mass spectra between peaks. The calculated H_2^+/H_2O^+ ratios of peak areas from m/z = 2 and m/z = 18 signals did not include differences in ionization efficiency of the molecules, thus the ratios do not correspond to weight or atomic relationships between the gases (Lampe et al. 1957); hence, the H_2^+/H_2O^+ trend was interpreted only semi-quantitatively. The coefficient of determination (R^2)

evaluated for the linear model of the relationship between the H_2O^+ (m/z 18) MS spectra and the DTG curves was based on simultaneous analysis related to the experiment time.

Infrared (IR) *in situ* experiments of SG7 and Sptb chlorites were conducted using a Praying Mantis (by Harrick, USA) diffuse reflection (DRIFT) accessory equipped with a high temperature reaction chamber. Spectra were collected using a Nicolet 6700 spectrometer with a DTGS KBr detector (Thermo Scientific, Waltham, Massachusetts, USA) with a 4 cm^{-1} resolution and 256-scan averages. Chlorite samples were mixed and ground with diamond powder (15% concentration), then gradually heated between 25 to ~ 800 °C under a dry nitrogen gas atmosphere (>99.999% purity) or synthetic air (>99.99% purity) with a 400 cm^3/min rate flow. Before collecting each spectrum, samples remained at the selected temperature for 30 minutes. Blank spectra (only with diamond powder) were collected for each temperature and time, using the same heating patterns as with the samples of interest. The protocol of *in situ* gradual heating of SG7 and Sptb via the Thermo-DRIFT method was designed to correspond to TG experiments. The structural OH-stretching region (2800-3800cm^{-1}) was selected as the most sensitive to the thermally-induced changes in the studied chlorites.

Results

TG-MS experiments under inert gas atmosphere.

Thermogravimetry. In agreement with previous studies (Prieto et al. 1991; Steudel et al. 2016; Lempart et al. 2018) the chlorites studied showed two steps of dehydroxylation involving the two octahedral sheets, which were observed as two events on TG and DTG curves between 400 and 900 °C (Fig. 1). The higher the Mg content in the chlorites, the higher the temperature of corresponding mass loss events. Total mass losses (Δm_{dx}) obtained under a 20°C/min rate to 1000 °C varied from 10.08 wt% for MtBl and 10.16 for SG7 to

12.81 wt% for POST (Tab. 2). The Δm_{dx} increased proportionally with Mg content and the decrease of Fe content. In general, the first thermal event corresponded to a much higher mass loss than the second event (more than the theoretical 3:1 ratio). Only for Fe-rich clinochlore - Sptb, was the ratio of DTG peak areas close to 2:1 (Fig. 1d). As shown on Figure 2, Δm_{dx} for chamosites and Fe-rich clinochlores was lower than the theoretical mass loss ($H_2O(+)$) calculated assuming that all OH groups dehydroxylated following Equation 1. The mass loss of biotite (LP-6), tested as a chlorite 2:1 layer analogue, was not complete at 1050 °C, which is the maximum temperature limit for the TG instrument (Figs. 3a, b). The DTG curve revealed a broad peak beginning at 700 °C with the maximum above 1000°C. The measured Δm_{dx} was 2.13 wt%, whereas the calculated $H_2O(+)$ of LP-6 was 3.50 wt%.

Mass spectrometry. Evolved gas analyses for ramp-heated chlorites showed H_2O (m/z = 18) evolution following weight changes on the TG curves (Fig. 1). In addition to releasing H_2O, H_2 (m/z = 2) evolution was observed for SG7, MtBl, CCa-2, Sptb, and Mal (minimal) samples, during ramp heating in N_2, and no H_2 evolution was observed for POST (Fig.1). H_2 and H_2O evolved between 550 – 810 °C for SG7 and MtBl, whereas for CCa-2 and Sptb the range was 610 to 900 °C. Also, the H_2 mass spectrum profile of biotite (LP-6) showed a broad peak between 640 and 1000 °C (Fig. 3b), which occurred prior to the main stage of H_2O evolution. The H_2O mass profile of LP-6 did not showed a well-defined peak with maximum below 1050 °C.

In all tested chlorites and biotite, the evolved molecules with m/z = 2 did not follow m/z = 18 or m/z = 17 (OH^+). No other volatiles were found to contribute to total mass losses during heating in nitrogen gas. The O_2 (m/z = 32) mass spectrum profile did not show any discrete peaks and only a slightly elevated background line was observed between 900 and 1000 °C for all the chlorites tested.

The ratio of H_2^+ and H_2O^+ total peak areas varied from 0.0019 for SG7 to 0.00025 for Mal and zero for POST (Tab. 2). Similarly to H_2O, H_2 mass spectrum profiles revealed two characteristic peaks (hereafter I and II), clearly distinguishable as two thermal events (Fig. 1). In the evolved H_2 spectrum, the ratio of two corresponding peak areas ($H_2^+{}_I/H_2^+{}_{II}$) varied from ~9 for SG7 and ~4 for MtBl, to ~2 and ~1 for CCa-2 and Sptb, respectively (Tab. 2). In all chlorites studied, except SG7, the $H_2^+{}_I/H_2^+{}_{II}$ ratio was lower than the corresponding $H_2O^+{}_I/H_2O^+{}_{II}$ ratio. A calculation of the H_2^+/H_2O^+ ratio for LP-6 did not yield realistic values, because the H_2O peak was poorly defined with incomplete H_2O release below 1050 °C.

The correlation of DTG and MS signals. The coefficient of determination (R^2) calculated for a linear correlation between the DTG curve and H_2O mass spectrum profile varied from 0.984 to 0.995 (Tab. 3). The relationship between the shape of the DTG curve and the H_2O mass spectrum profile of LP-6 was $R^2 = 0.922$ and indicated a quasi-linear regression (Tab. 3).

Mössbauer spectroscopy. In the chlorites heated by TG to 1000 °C, the Fe(III) content increased with respect to the natural samples (Tab. 4, Supplemental Fig.S1). For heated CCa-2, Sptb, and Mal, the assignment of the fitted parameters of isomer shift (IS) and quadrupole splitting (QS) allowed Fe(II) and Fe(III) components to be clearly distinguished, in contrast to chamosites where the interpretation of the fitted parameters was not clear. The chamosites showed new doublets represented by IS = 0.84 mm/s, QS=1.58 mm/s in SG7 and IS=1.04 mm/s, QS=1.18 mm/s, in MtBl, which were interpreted following Dyar et al. (2006) as the mixed-valence Fe(II)-(III) doublet (Fe(II) - (III) in Table 4). For heated CCa-2, Sptb, and Mal, the assignment of separate Fe(II) and Fe(III) doublets after *f* fraction correction showed approximately 21%, 22%, and 4% of newly formed Fe(III) ($\Delta Fe(III)_{Cf}$), respectively (see the evaluation approach in Supplemental Information). For the chamosites SG7 and MtBl, the component clearly corresponding to Fe(III) showed ~ 7% of $\Delta Fe(III)_{Cf}$ (Tab. 4). However, the

mixed-valence Fe(II)-(III) doublet in chamosites did not allow the correction of measured Fe(II) and Fe(III) contents with respect to *f* (Supplemental Information). The measurements performed for heating the reaction product of LP-6 showed 74% of $\Delta Fe(III)_{Cf}$ (Tab. 4, Supplemental Fig. S1).

Isothermal heating (cf. Lempart et al. 2018). Isothermal heating at 400 °C for 48h was intended to produce advanced dehydrogenation prior to the following ramp heating segment (Lempart et al. 2018). In contrast to MtBl heated only under ramp conditions (Fig. 1a), in the post-isothermal ramp heating segment the evolved gas analysis revealed only H_2O release; no H_2 release was observed (Fig. 4). The H_2O mass spectrum profile showed a peak matching the DTG peak. During the isothermal segment the volatiles could not be analyzed in the MS system because the reaction progressed too slowly to obtain a sufficient MS signal.

TG-MS experiments under oxidizing gas atmosphere

Thermogravimetry. In addition to the expected decrease in Δm_{dx} in air for Fe(II)-containing chlorites with respect to heating in nitrogen gas (Fig. 2), Fe-rich chlorites heated in synthetic air also showed a change in the shape of DTG peaks (Tab. 2, Fig. 1). In contrast to the two-step thermal decomposition observed for an inert gas (N_2), in the Fe(II)-rich chlorites SG7, MtBl, and CCa-2 only one, broader DTG peak remained, whereas the second peak observed on DTG curves recorded under N_2 at 700–820 °C, nearly disappeared. However, for Sptb, the DTG peak located at 821 °C in N_2 split to peaks at 772 °C and 859 °C. Moreover, for SG7 a low-temperature shoulder of the first major DTG peak appeared at ~480 °C. As observed under N_2, the mass loss of biotite (LP-6) under oxidizing gas was not completed at 1050 °C. At 1050 °C, Δm_{dx} was 1.54 wt% (Figs. 3c, d) whereas the onset of mass loss occurred near 900 °C, which was much higher than under nitrogen gas (*cf*. Figs.3a and 3c).

312 **Mass spectrometry.** H_2O (m/z=18) gas evolution was observed for all chlorites and biotite
313 tested (Fig. 1, Fig. 3), however, no H_2 (m/z = 2) gas evolution was detected for any of the
314 chlorites and biotite heated in air. In SG7, Mal, POST, and LP-6, the CO_2 (m/z = 44) mass
315 spectrum profile showed a small, broad peak between 300 and 600 °C, most likely originating
316 from the oxidation of trace organic compounds. A second peak was found at 900 °C, which
317 corresponds to the decarbonatization of trace carbonate minerals. The contribution of CO_2 gas
318 to DTG and also Δm_{dx}, was negligible in comparison to evolved H_2O (maximum CO_2^+/H_2O^+ =
319 0.0129). Volatile SO_2 (m/z=64) was detected for only SG7 as a sharp peak at 600 °C with a
320 negligible contribution to Δm_{dx}, (SO_2^+/H_2O^+ =0.0002). The SO_2 was probably related to
321 oxidation of pyrite impurities undetectable in XRD.

322 **The correlation of DTG and MS signals.** Except for SG7 and LP-6, the shape of H_2O mass
323 spectrum profiles closely corresponded to that of the DTG curves, with R^2 varying from 0.953
324 to 0.997, for Sptb and POST, respectively (*cf.* Fig. 1, Fig. 5 and Tab. 3). The shape of the H_2O
325 mass spectrum profile of SG7 strongly differed from the DTG curve shape resulting in an R^2
326 of 0.603 (Fig. 5, Tab. 3). The H_2O spectrum revealed two pronounced peaks: a larger peak at
327 464 °C and a smaller peak at 547 °C, whereas the DTG curve showed only one major, broad
328 peak at 545 °C with a low-temperature shoulder (Fig. 1a). The H_2O mass spectrum profile of
329 LP-6 revealed a low-temperature peak at 300 °C corresponding to the DTG curve, and a broad
330 peak at 620 °C that was accompanied by a disproportionally weaker DTG peak (Fig. 3d).
331 Similar to SG7, LP-6 biotite did not show a high correlation between the DTG curve and the
332 H_2O mass spectrum profile, resulting in an R^2 of 0.879 (Tab. 3). A low-temperature DTG
333 peak near 300 °C matched the CO_2 mass spectrum profile and was therefore associated with
334 the oxidation of trace organic impurities. Also, the H_2O mass spectrum profile of Sptb showed
335 three pronounced peaks at 668 °C, 772 °C, and 860 °C, with a low-temperature shoulder near

620 °C, whereas the DTG curve showed different proportions and shapes for these three peaks (Fig. 1d).

Mössbauer spectroscopy. Mössbauer spectroscopy measurements indicated complete oxidation of Fe(II) in selected analyzed chlorites after heating to 1000 °C in air (Tab. 4).

TG-MS of chamosite combining oxidizing and inert gas atmosphere

To investigate the variation in the shape of the H_2O and DTG profiles of SG7, a ramp-heating experiment for SG7 involving switching the gases (air and N_2) was performed (Fig. 6). The experiment started with ramp-heating with a 20°C/min rate in synthetic air to a temperature of 460 °C, corresponding to the first peak in the H_2O mass spectrum profile observed under synthetic air (*cf.* Fig. 1a). Then, the oxidizing gas was switched to nitrogen and ramp heating continued to 1000 °C. In this two-gas atmosphere, the H_2O mass spectrum profile revealed two peaks at 460 °C and 515 °C, and H_2 was not detected in the synthetic air step or under nitrogen (*cf.* Fig. 1a and Fig. 6).

Thermo-DRIFT experiments

The protocol of *in situ* gradual heating of SG7 and Sptb via the Thermo-DRIFT method corresponds to thermogravimetric experiments (*cf.* Figs.1a, d and Fig. 7). In unheated samples, bands at 3660 – 3618 cm^{-1} originate from OH groups bonded to the cations in the 2:1 layer, mostly Mg and Fe^{2+} ($OH_{2:1}$ in Fig.7a) (Shirozu 1985; Bishop et al. 2008). Two broad bands near 3545 and 3418 cm^{-1} are associated with H bonds of OH groups in the interlayer octahedral sheet interacting with the tetrahedral sheet, commonly described as (SiSi)O-OH and (SiAl)O-OH (OH_{int} in Fig.7a) (Hayashi and Oinuma 1967; Shirozu 1980).

SG7 heated to 500 °C in a nitrogen gas atmosphere showed some reduction of OH_{int} bands and smoothing of the band near 3618 cm^{-1} ($OH_{2:1}$), followed by a simultaneous, steady

359 decrease in all OH bands in both the interlayer and the 2:1 layer at higher temperatures (Fig.
360 7a). Heating under synthetic air revealed a different order of OH band decrease (Fig. 7b).
361 Until 300 °C, the spectra resembled those at 25 °C, but above 300 °C a rapid change was
362 observed. The band at 3618 cm^{-1} disappeared, whereas the band at 3418 cm^{-1} was strongly
363 reduced and a broad complex band at 3530 cm^{-1} occurred. This broad band was present after
364 heating at 650 °C. As a result of analytical problems, high quality spectra of SG7 could not be
365 obtained under air at temperatures of > 650 °C.

366 Sptb heated to 600 °C in nitrogen gas showed a small reduction in OH_{int} band intensity
367 (Fig. 7c). The greatest reduction in these bands was observed after heating at 700 °C.
368 However, at 750 °C, a broad OH_{int} band near 3421 cm^{-1} remained. Heating at 860 °C left only
369 two distinguishable bands: 3644 cm^{-1} and 3620 cm^{-1} ($OH_{2:1}$). Minor differences were noted
370 between Sptb heated under N_2 gas and synthetic air (Figure 7d). Stronger reductions in OH_{int}
371 bands were observed at 750 °C, whereas at 800 °C a broader and more complex band was
372 present in the 3640 to 3540 cm^{-1} region.

373 ## Discussion

374 ### H_2 gas liberation as the indicator for dehydrogenation

375 Evolved H_2 in all mineralogically pure Fe(II)-containing chlorites and biotite heated
376 under an inert gas atmosphere is consistent with that dehydrogenation producing H_2 gas. The
377 quantitative correlation of H_2 evolution with H_2O and Fe(II) content in chlorites (Fig. 2),
378 including the absence of H_2 in clinochlore (Fig. 1f), is consistent with Equation 3. Along with
379 different ratios between $H_2^+{}_I/H_2^+{}_{II}$ and $H_2O^+{}_I/H_2O^+{}_{II}$ (Tab. 2), and the lack of daughter ions in
380 H_2O mass profiles, the H_2^+/H_2O^+ variability ruled out the production of the m/z = 2 signal by
381 fragmentation of H_2O (*cf.* Steudel et al. 2016). Due to differences in ionization efficiency and
382 the lack of a gas H_2^+/H_2O^+ ratio standard for MS measurement, the observed H_2^+/H_2O^+ ratio

suggests a semi-quantitative interpretation of dehydrogenation. However, the evolved gas ratio of H_2^+/H_2O^+ with a general trend of an increase in Fe(III) or Fe(II,III) content (*cf.* Tab. 2 and Tab. 4) and the reduction in total mass losses (dehydroxylation) resulting with concurrent dehydrogenation (Fig. 2) indicate that the interpretation of the H_2 release is correct.

Despite fast-ramp heating (rate of 20°C/min), which in Lempart et al. (2018) favored dehydroxylation over dehydrogenation, pronounced dehydrogenation occurred in Fe(II)-containing chlorites and caused the corresponding oxidation of structural Fe(II) (Tab. 4). When the isothermal heating procedure, which highly enhances dehydrogenation over dehydroxylation, was applied (following Lempart et al. (2018)), the lack of H_2 liberation during the subsequent ramp heating stage was evidence that all Fe(II) available for dehydrogenation must had been oxidized (Fig. 4). The heating procedure: static or dynamic, resulted in the enhancement or limitation of dehydrogenation, respectively, but only fast ramp heating provided evidence to interpret dehydrogenation by measurable amounts of H_2 gas.

Determination of the degree of oxidation

The mixed valence Fe(II,III) component did not permit accurate determination of newly formed Fe(III) for heated chamosites (Tab. 4, Supplemental Fig. S1), and therefore evolved H_2 and ΔFe(III) could not be determined. Based on Ferrow et al. (1988), Burns (1991), and Dyar et al. (1998, 2006) works describing electron delocalization in Fe-rich minerals, Fe(II,III) represents electron hopping between adjacent Fe(II) and Fe(III) atoms. Therefore, an unknown portion of the Fe(II,III) component may be assigned to the total Fe(III). Fe(III) may represent the hercynite and fayalite contaminants in the recrystallization product of chamosite (Supplemental Fig. S2). Fe(III)-bearing hercynite contains Fe (II,III) pairs and clusters prone to an electron transition in octahedral coordination (Hålenius et al. 2002), that may explain the Fe(II,III) component in Mössbauer spectroscopy results.

Additional uncertainties inherent to Mössbauer spectroscopy may result from the unknown content of the recoil-free fraction in our samples, which did not allow a reliable determination of Fe(II)/Fe(III) ratio (see evaluation approach in Supplemental Information).

Concurrent H_2 and H_2O release events

The same temperature interval for H_2 and H_2O evolution, occurring as a two-step reaction for all Fe(II)-containing chlorites during ramp heating showed that dehydrogenation and dehydroxylation proceeded simultaneously. However, the difference in the $H_2O^+_I/H_2O^+_{II}$ and $H_2^+_I/H_2^+_{II}$ ratios and various shapes and intensity of H_2 and H_2O peaks on mass profiles demonstrated that these reactions proceed with independent mechanisms. Despite ramp-heating conditions, these reactions proceed similar to isothermal conditions, as described by Lempart et al. (2018). However, the proximity of the H_2O and H_2 peaks, and with most H_2 release not occurring before the onset of dehydroxylation (Fig. 1 and 3), suggest that dehydroxylation may either trigger dehydrogenation or enhance its rate. In turn, dehydrogenation can only limit dehydroxylation by removing OH groups available for dehydroxylation (see Fig. 2). The contribution of evolved hydrogen to mass loss is negligible (H_2 equals 1/9 wt. of H_2O), therefore H_2O release controls mass loss. Indeed, the high coefficient of determination (R^2) for a linear correlation between the DTG curve and H_2O mass spectrum profile (Tab. 3), proves that dehydroxylation controls mass loss under an inert gas atmosphere. Similar overlap of H_2O and H_2 evolution was observed by Norman and Palin (1982) for chlorite, biotite, and muscovite; MacKenzie et al. (1986) for minnesotaite, and Rouxhet et al. (1972) for amphiboles and biotite. Hence, the concurrent, but independent model of H_2 and H_2O liberation is applicable for all Fe(II)-containing phyllosilicates regardless of different structural features (e.g., vacancies in biotite or mode of layer stacking in chlorites).

431 **Dehydrogenation in the 2:1 layer and the interlayer sheet**

432 Two events revealed as subsequent H_2^+ and H_2O^+ MS peaks were tentatively
433 associated with reactions in the interlayer and the 2:1 layer, respectively (Eqs. 2a and 2b).
434 Whereas in clinochlores and Fe-rich clinochlores the $H_2O^+_I/H_2O^+_{II}$ ratio remained close to the
435 theoretical 3:1 ratio, chamosites had a ratio to twice as high. For dehydrogenation, the
436 $H_2^+_I/H_2^+_{II}$ ratio linearly follows the structural Fe(II) content, starting from a nearly equal
437 distribution between the two thermal events for Fe-rich clinochlore, to a predominance of the
438 low-temperature effect in chamosite.

439 Mg-rich chamosite (MtBl) heated under isothermal conditions at 400 °C, which is the
440 temperature for dehydroxylation of the interlayer sheet, resulted in nearly complete loss of
441 OH groups associated with dehydroxylation of the 2:1 layer at higher temperature (Fig. 4). If
442 the 2:1 layer of chlorite contains a significant number of $2Fe^{2+}R^{2+}OH$ clusters (as in
443 chamosite), not all H_2 evolved during low-temperature events can be unequivocally assigned
444 to only the interlayer sheet, but H_2 may evolve also from the 2:1 layer. Because
445 dehydroxylation and dehydrogenation destabilizes the crystal structure, and likely proceeds
446 sheet-by-sheet (in the interlayer sheet and the 2:1 layer) to produce mixed-layering (Lempart
447 et al. 2018), the 2:1 layers adjacent to the dehydroxylated and partially dehydrogenated
448 interlayer are likely more susceptible to electron transfer than the intact structure. This
449 explanation may be the reason why Ross and Kodama (1974) and Goodman and Bain (1979)
450 observed unexpected oxidation of Fe(II) in the 2:1 layer during thermal treatment that should
451 only decompose the interlayer octahedral sheet of chlorites.

452 In contrast to chlorites, for biotite, considered analogous to the 2:1 layer in chlorites,
453 H_2 liberation was completed before dehydroxylation reached the maximum. Also, biotite
454 underwent almost complete oxidation, 74 % $\Delta Fe(III)_{Cf}$ with respect to only 22 % $\Delta Fe(III)_{Cf}$ in

455 the compositionally closest Fe-rich clinochlore (Sptb). These observations imply that the
456 primary control on the mass loss pattern upon dynamic heating for Fe(II)-rich chlorite is
457 dehydrogenation of the 2:1 layer that occurs before its dehydroxylation. Indeed, Charsley et
458 al. (1987) observed a unique high-temperature H_2 peak in ramp-heated "ripidolite" (Fe-rich
459 clinochlore), whereas H_2O was released in two-steps, implying that H_2 release (therefore
460 Fe(II) oxidation) occurs only in the 2:1 layer.

461 The $H_2^+{}_I/H_2^+{}_{II}$ ratio is controlled by two factors: a) total Fe(II) content and its
462 distribution between the two octahedral sheets, and b) the conditions required to
463 dehydrogenate a given population under dynamic heating conditions. Therefore, two separate
464 H_2 peaks indicate only qualitatively that Fe(II) occurs in both octahedral sheets in positions
465 prone to dehydrogenation before dehydroxylation under ramp heating.

466 The tendency of the 2:1 layer to dehydrogenation produces differences in the order of
467 thermal decomposition between Fe-rich clinochlore and chamosite as shown by IR spectra
468 (Fig. 7). For Fe-rich clinochlore heated under inert gas, the boundary between the
469 decomposition of the interlayer and the 2:1 layer octahedral sheets was clearly distinguishable
470 (~750 °C). For chamosite, the decomposition of both sheets was simultaneous, and the
471 boundary temperature between the two steps was essentially absent. Under synthetic air, the
472 readily observable disappearance of the high-temperature event on DTG curves for Fe(II)-rich
473 chlorites and the $OH_{2:1}$ stretching FTIR band of chamosite (*cf.* Fig.1 and Fig.7) suggests that
474 dehydrogenation (Equation 4) consumed all OH groups in the 2:1 layer before
475 dehydroxylation (Lempart et al. 2018). In contrast, the corresponding TG and DRIFT features
476 in Fe-rich clinochlore (Sptb) heated under air (Fig. 1c; Fig. 7), closely resembled those under
477 inert gas (Fig. 1f, Fig. 5). Consequently, a widely accepted model for the thermal
478 decomposition order of chlorite layers, where dehydroxylation of the interlayer's octahedral

sheet is followed by that of the 2:1 layer resulting in two discrete thermal events (e.g., Zhan and Guggenheim 1995; *cf.* Moore and Reynolds 1997) is not applicable for chamosites.

The role of oxygen in dehydrogenation

Hydrogen cannot be detected using MS for any sample heated under an oxidizing gas, because hydrogen, if released, will combine with oxygen to form H_2O, following Equation 4 (Fig. 1). An oxygen-rich atmosphere is expected to enhance both dehydrogenation and Fe(II) oxidation (Sanz et al. 1983; MacKenzie et al. 1986; Rancourt et al. 1993). However, oxidation is not driven by bonding residual oxygen anions within the structure following Equation 5 as widely considered. Any oxidation following Equation 5 that occurs before dehydroxylation should cause mass gain (as observed by Rancourt et al. 2001, *cf.* Lempart et al. 2018), which was not observed by TG curves (Figs. 1 and 3). Prior to complete dehydroxylation and phase transformation (required for trioctahedral phases), O_2 does not diffuse through the phyllosilicate structure and does not bond directly to Fe(II) sites (Tripathi et al. 1978). The oxidation described by Equation 5 occurs only after Fe is exposed to the oxidative atmosphere, i.e. after dehydroxylation and structural transformation (Rouxhet et al. 1972), and after the collapse of the layer structure that screens Fe from contact with O_2. If a Fe(II)-rich chlorite is heated under inert gas, dehydrogenation proceeds only following Equation 3, whereas providing oxygen to the reaction products at 1000 °C causes oxidation following Equation 5 (Lempart et al. 2018). However, when ramp-heated under oxidizing conditions, the structure dehydrogenates completely (following Equation 4) before dehydroxylation. The resulting structure that forms during dehydroxylation immediately reacts with surrounding oxygen and consequently produces fully oxidized Fe(II). These two different processes result in the same final mass loss, making them indistinguishable via TG analysis (Lempart et al. 2019).

If preceded by ramp-heating under air to 460 °C (thus before the onset of dehydrogenation under N_2), the m/z=2 mass spectrum of chamosite did not show H_2 evolution (Fig. 6) despite overlapping H_2 and H_2O peaks recorded under N_2 gas (Fig. 1a). Therefore, all the H_2 must have been released at a lower temperature, under air, where it produced an additional H_2O MS signal, which was not matched by mass loss in the DTG curve profile (Fig. 5). The same result was observed for chamosite and biotite heated only under air. In result, dehydrogenation completed before dehydroxylation produced a MS signal of water molecules with a maximum near 480 °C and 620 °C, respectively, with no corresponding signal in the DTG curve (Fig. 1 and Fig. 3). The consequence of this mismatch was the lack of a linear correlation between MS and DTG curves (Tab. 3, Fig. 5). If heated in the absence of oxygen (in N_2 gas), these two samples dehydrogenated at the temperature ~ 150 °C higher and needed some kind of trigger, such as dehydroxylation, to proceed (Fig. 1a; Fig. 3). The migration of hydrogen (either as H_2 or as H radical) to the crystal surface causes a near immediate reaction with externally derived oxygen to form water molecules in the carrier gas according to Equation 4 (MacKenzie and Berezowski 1981, 1984; Borggaard et al. 1982) without producing the mass loss corresponding to dehydroxylation.

In chlorites heated under air (except for SG7) close linear correlation between DTG and H_2O data was observed, resulting from dehydroxylation that overlapped with dehydrogenation. Therefore, enhanced production of H_2O could not appear in the MS as an additional peak (Tab. 3). However a perfect linear correlation in the oxidizing gas atmosphere, was observed only for POST due to a sole dehydroxylation controlling mass loss (Figs. 5c, d).

Potential mechanisms of dehydrogenation

Among the proposed mechanisms of dehydrogenation one included a hopping of protons and electrons travelling separately to the mineral surface, as found mainly in amphiboles (e.g., Addison and Sharp 1962) and also in biotite (Hogg and Meads 1975). In another suggested process a hydrogen radical atom, or a close association of a proton and an electron diffuses through the crystal structure to the surface (Vedder and Wilkins 1969; Rouxhet et al. 1972). Unfortunately, the detection and quantification of hydrogen evolved as H_2 gas does not allow identifying the site where H_2 molecule formation: either within the crystal or at the crystal surface.

The initial formation of H_2 from H radicals released during dehydrogenation from neighboring OH sites coordinated to Fe(II) seems the most energetically favorable reaction. If formed within a crystal, however, the H_2 molecule would need to diffuse through a closely packed atomic structure. Dehydroxylation that results from H_2O migration out of the crystal through the interlayer requires an interlayer spacing with a width greater than the effective diameter of H_2O (~ 3.0 Å), which would also be sufficient for H_2 (~2.3 Å kinetic and ~2.9 Å van der Waals diameter). The observed close association of H_2O and H_2 release may be related to the restriction of H_2 transfer throughout the crystal structure, similar to H_2O. Therefore, close H_2O and H_2 release association implies that these two compounds migrate as H_2O and H_2 through the crystal structure where the interlayer is sufficiently open. Rehydrogenation observed under H_2 gas flow for Fe-rich clinochlore (Borggaard et al. 1982) at temperatures appropriate for the onset of dehydroxylation also demonstrate that H_2 can migrate through the chlorite structure. From a kinetic standpoint, in the 2:1 layer, the activation energy for dehydrogenation of biotite and Fe-rich phlogopite (194 and 228 kJ/mol; Rancourt et al. 1993 and Zema et al. 2010, respectively) is near to that of the dehydroxylation of kaolinite (228 kJ/mol; Redfern 1987) or smectites (159-249 kJ/mol; e.g. Kuligiewicz and Derkowski 2017). Dehydrogenation and dehydroxylation are controlled by the dissociation of

551 structural OH groups, however, the higher energy required to dehydroxylate and transform the
552 trioctahedral structure enables dehydrogenation to proceed as a kinetically-controlled process
553 before dehydroxylation advances (*cf.* Lempart et al. 2018).

554 Under oxidizing conditions, O_2 at the surface is a sink for the electron of the hydrogen
555 radical, thus facilitating the migration of hydrogen radicals to the surface, where H_2O is first
556 formed, without requiring H_2 to form (*cf.* Tripathi et al. 1978; Sanz et al. 1983). When
557 external O_2 is present, the reaction equilibrium shifts and the reaction occurs at a lower
558 temperature, in contrast to inert gas condition, when another hydrogen radical acts as an
559 electron donor-acceptor to form H_2.

560 In addition to the presence of external oxygen, the distribution of octahedral cations
561 influences the pathway of dehydrogenation and its relation to dehydroxylation (Lempart et al. 2018).
562 Also, chlorite's stacking disorder, which generates tetrahedral rotations and polyhedral
563 distortions (Walker and Bish 1992; Zhan and Guggenheim 1995), and the interstratyfication
564 of polytypes can weaken hydrogen bonds between the interlayer and the 2:1 layer, thus
565 facilitating dehydroxylation and dehydrogenation in Fe(II)-containing chlorites. Among all
566 studied chlorites only SG7 underwent dehydrogenation prior to dehydroxylation under
567 oxidizing conditions (compare Figs. 1a and 1b). By coincidence or not, SG7 is also
568 structurally unique among all the studied samples, having the highest fraction of polytypes
569 different than IIbb (19%), and ~ 40% of layers not shifted by ±1/3b (cf. Luberda-Durnaś et al.
570 2019).

571 **Implications**

572 Under oxidizing atmosphere, ions monitored by evolved gas analysis can represent
573 both original volatiles evolved from a sample and volatiles newly formed outside of the
574 sample by a reaction with a carrier gas, whereas TG and DTG curves are affected only by

reactions inside the sample. As shown in Figure 5, any contact of Fe(II)-bearing phyllosilicates with external oxygen, when heated to high-temperature, will produce an H_2O signal that does not originate from dehydration or dehydroxylation of the mineral (Equation 1), but from dehydrogenation following Equation 4 (*cf.* Morgan et al. 1988; Steudel et al. 2016). The MS signal of H_2O would be misleading if used as a proxy for monitoring the progress of H_2O evolution. For analysing dehydration and dehydroxylation of Fe(II)-bearing minerals, the use of thermogravimetric data is recommended. MS curves can be used as a reaction proxy only after correlation with TG data (Fig. 5) to provide a consistent interpretation of both analyses.

The combination of TG analysis and MS for evolved gas analysis provides a better understanding of dehydrogenation and dehydroxylation showing quantitatively that all Fe(II)-bearing phyllosilicates produced H_2 by oxidative dehydrogenation. Evolved gas analysis with MS is used by the Curiosity Rover on Mars, heating rocks to 835 °C (Archer et al. 2014; Ming et al. 2014). Based on our observations and interpretations, H_2 and H_2O evolution at high temperatures (~550 °C and 700 to 800 °C) may be used as a diagnostic tool of Fe(II)-bearing phyllosilicates on Mars (*cf.* Ming et al. 2014). Moreover, the presence of Fe(II)-rich phyllosilicates on Mars implies the probability of dehydrogenation, which may have affected the hydrogen budget on its surface (Burt 1989).

Experiments on Mg-Fe chlorites heated in an inert and oxidizing gas atmosphere can closely reflect an anaerobic and aerobic geological environment, respectively. However, as shown here, the $Fe(III)/Fe_{total}$ ratio does not directly reflect oxygen fugacity. The occurrence of oxidative dehydrogenation complicates interpretations based on not only the valence of Fe, but also that of other common octahedral cations in phyllosilicates e.g. Mn (Tyrna and Guggenheim 1991) in understanding the role of oxygen fugacity and redox conditions in rock and mineral formation (Dyar et al. 1993; Feeley and Sharp 1996). Therefore, the investigation

of chemical and isotopic composition of phyllosilicates to model the above processes, should include an accurate estimation of Fe^{3+}/Fe^{2+} ratio and hydrogen content (Dyar et al. 1996; Demeny et al. 2006; Brounce et al. 2014). As recommended by Lempart et. al (2018) and Masci et al. (2019), the structural formula of Fe(III) containing chlorite should not be calculated without considering the loss of protons. Also oxidative dehydrogenation may bias thermodynamic calculations for phyllosilicates used as geothermobarometers for retrieving P/T conditions of subduction and exhumation events.

In descending continental slabs in subduction zones, potential dehydrogenation of Fe(II)-bearing phyllosilicates affects the pathways of fluids released during deep burial and changes the budget of water and H_2 gas in metamorphic and magmatic processes (Schmidt and Poli 1998; Grove et al. 2006). Additionally, studies involving thermal H_2 desorption from minerals (e.g. Truche et al. 2018) should consider dehydrogenation and rehydrogenation as potential effects, which influence the apparently adsorbed H_2 content and isotope composition.

Acknowledgments

This study was funded by the National Science Centre Poland under research project no. 2017/27/N/ST10/02544.

References

Addison, W.E., and Sharp, J.H. (1962) A mechanism for the oxidation of ferrous iron in hydroxylated silicates. Clay Minerals, 5, 73–79.

Aja, S.U., and Dyar, M.D. (2002) The stability of Fe-Mg chlorites in hydrothermal solutions - I. Results of experimental investigations. Applied Geochemistry, 17, 1219–1239.

Archer, P.D., Franz, H.B., Sutter, B., Arevalo, R.D., Coll, P., Eigenbrode, J.L., Glavin, D.P., Jones, J.J., Leshin, L.A., Mahaffy, P.R., and others (2014) Abundances and implications of volatile-bearing species from evolved gas analysis of the Rocknest aeolian deposit, Gale Crater, Mars. Journal of Geophysical Research: Planets, 119, 237–254.

Bayliss, P., Kaesz, H.D., and Nickel, E.H. (2005) The use of chemical-element adjectival modifiers in mineral nomenclature. The Canadian Mineralogist, 43, 1429–1433.

Bishop, J.L., Lane, M.D., and Dyar, M.D. (2008) Reflectance and emission spectroscopy study of four groups of phyllosilicates : smectites, kaolinite-serpentines, chlorites and micas. Clay Minerals, 43, 35–54.

Borggaard, O.K., Lindgreen, H.B., and Morup, S. (1982) Oxidation and reduction of structural iron in chlorite at 480 °C. Clays and Clay Minerals, 30, 353–363.

Brett, N.H., MacKenzie, K.J.D., and Sharp, J.H. (1970) The thermal decomposition of hydrous layer silicates and their related hydroxides. Quarterly Reviews, Chemical Society, 24, 185–207.

Brounce, M.N., Kelley, K.A., and Cottrell, E. (2014) Variations in $Fe^{3+}/\sum Fe$ of Mariana Arc Basalts and MantleWedge fO_2. Journal of Petrology, 55, 2514–2536.

Burns, R.G. (1991) Mixed valency minerals: influences of crystal structures on optical and Mössbauer spectra. Applications in Chemistry, Physics and Biology, 175–199.

Burt, D.M. (1989) Iron-rich clay minerals on Mars: potential soures or sinks for hydrogen and indicators of hydrogen loss over time. Proceedings of the 19th Lunar and Planetary Science Conference, 423-432.

Charsley, E.L., Manning, N.J., and Warrington, S.B. (1987) A new integrated system for simultaneous TG-DTA-MASS spectrometry. Thermochimica Acta, 114, 47–52.

Chrisman, B.L., and Tumolillo, T.A. (1971) Computer analysis of Mössbauer spectra. Computer Physics Communications 2, 2, 322–330.

Deer, W.A., Howie, R.A., and Zussman, J. (1992) An introduction to the rock forming minerals, 340-343 p. Longman, Harlow.

De Grave, E., and Van Alboom, A. (1991) Evaluation of Ferrous and Ferric Miissbauer Fractions. Physics and Chemistry of Minerals, 337–342.

Demeny, A., Vennemann, T.W., Harangi, S., Homonnay, Z., and Forizs, I. (2006) H_2O- δD-FeIII relations of dehydrogenation and dehydration processes in magmatic amphiboles. Rapid Communication in Mass Spectroscopy, 20, 919–925.

Drits, V.A., Besson, G., and Muller, F. (1995) An improved model for structural transformation of heat-treated aluminous dioctahedral 2:1 layer silicates. Clays and Clay Minerals, 43, 718–731.

Dyar, M.D., Guidorttri, C.V., Holdaway, M.J., and CoLucci, M. (1993) Nonstoichiometric hydrogen contents in common rock-forming hydroxyl silicates. Geochimica et Cosmochimica Acta, 57, 2913–2918.

Dyar, M.D., Martin, S., Mackwell, S., Carpenter, S., Grant, C.A., and Mcguire, A.V. (1996) Crystal chemistry of Fe^{3+}, H^+, and D/H in mantle-derived augite from Dish Hill: implications for alteration during transport. Mineral Spectroscopy, a tribute to R. G. Burns, 5, 289–304.

Dyar, M.D., Taylor, M.E., Lutz, T.M., Francis, C.A., Guidotti, C.V., and Wise, M. (1998) Inclusive chemical characterization of tourmaline: Mössbauer study of Fe valence and site occupancy. American Mineralogist, 83, 848–864.

Dyar, M.D., Agresti, D.G., Schaefer, M.W., Grant, C.A., and Sklute, E.C. (2006) Mössbauer spectroscopy of Earth and Planetary materials. The Annual Review of Earth and Planetary Science, 34, 83–125.

Dyar, M.D., Schaefer, M.W., Sklute, E.C., and Bishop, J.L. (2008) Mössbauer spectroscopy of phyllosilicates: effects of fitting models on recoil-free fractions and redox ratios. Clay Minerals, 43, 3–33.

Ehlmann, B.L., Mustard, J.F., Clark, R.N., Swayze, G.A., and Murchie, S.L. (2011) Evidence

for low-grade metamorphism, hydrothermal alteration, and diagenesis on Mars from phyllosilicate mineral assemblages. Clays and Clay Minerals, 59, 359–377.

Farmer, V.C., Russell, J.D., McHardy, W.J., Newman, A.S.D., Ahlrichs, J.L., and Rimsaite, J.Y.H. (1971) Evidence for loss of protons and octahedral iron from oxidized biotites and vermiculites. Mineralogical Magazine, 38, 121–137.

Feeley, T.C., and Sharp, Z.D. (1996) Chemical and hydrogen isotope evidence for *in situ* dehydrogenation of biotite in silicic magma chambers. Geology, 24, 1021–1024.

Ferrow, E.A., Annersten, H., and Gunawardane, R.P. (1988) Mössbauer effect study on the mixed valence state of iron in tourmaline. Mineralogical Magazine, 52, 221–228.

Foster, M.D. (1962) Interpretation of the composition and a classification of the chlorites. U.S. Geological Survey Professional Paper, 414–A, 1–33.

Goodman, B.A., and Bain, D.C. (1979) Mössbauer spectra of chlorites and their decomposition products. Developments in Sedimentology, 27, 65–74.

Goto, A., and Tatsumi, Y. (1990) Stability of chlorite in the upper mantle. American Mineralogist, 75, 105–108.

Grove, T.L., Chatterjee, N., Parman, S.W., and Médard, E. (2006) The influence of H_2O on mantle wedge melting. Earth and Planetary Science Letters, 249, 74–89.

Grove, T.L., Till, C.B., and Krawczynski, M.J. (2012) The role of H_2O in subduction zone magmatism. Annual Review of Earth and Planetary Sciences, 40, 413–439.

Guggenheim, S., Adams, J.M., Bain, D.C., Bergaya, F., Brigatti, M.F., Drits, V.A., Formoso, M.L.L., Galán, E., Kogure, T., and Stanjek, H. (2006) Summary of recommendations of nomenclature committees relevant to clay mineralogy: report of the Association Internationale pour l'Etude des Argiles (AIPEA) Nomenclature Committee for 2006. Clays and Clay Minerals Minerals, 54, 761–772.

Hålenius, U., Skogby, H., and Andreozzi, G.B. (2002) Influence of cation distribution on the optical absorption spectra of Fe^{3+}-bearing spinel s.s.-hercynite crystals: Evidence for electron transitions in $^{VI}Fe^{2+}$-$^{VI}Fe^{3+}$ clusters. Physics and Chemistry of Minerals, 29, 319–330.

Hayashi, H., and Oinuma, K. (1967) Si-O absorption band near 1000 cm^{-1} and OH absorption bands of chlorite. The American Mineralogist, 52, 1206–1210.

Heide, K., and Földvari, M. (2006) High temperature mass spectrometric gas-release studies of kaolinite $Al_2[Si_2O_5(OH)_4]$ decomposition. Thermochimica Acta, 446, 106–112.

Heller-Kallai, L. (1997) The nature of clay volatiles and condensates and the effect on their environment. Journal of Thermal Analysis, 50, 145–156.

Heller-Kallai, L., Miloslavski, I., and Grayevsky, A. (1989) Evolution of hydrogen on dehydroxylation of clay minerals. American Mineralogist, 74, 1976–1978.

Hogg, C.S., and Meads, R.E. (1975) A Mössbauer study of thermal decomposition of biotites. Mineralogical Magazine, 40, 79–88.

Ingamells, C.O., and Engels, J.C. (1976) Preparation, analysis, and sampling constants for a biotite. U.S. National Bureau of Standards Special Publiction, 422, 403–419.

Kodama, H., Longworth, G., and Townsend, M.G. (1982) A Mössbauer investigation of some chlorites and their oxidation products. Canadian Mineralogist, 20, 585–592.

Kuligiewicz, A., and Derkowski, A. (2017) Tightly bound water in smectites. American Mineralogist, 102, 1073–1090.

Lampe, F.W., Franklin, J.L., and Field, F.H. (1957) Cross sections for ionization by electrons. Journal of the American Chemical Society, 79, 6129–6132.

Lempart, M., Derkowski, A., Luberda-Durnaś, K., Skiba, M., and Błachowski, A. (2018) Dehydrogenation and dehydroxylation as drivers of the thermal decomposition of Fe-chlorites. American Mineralogist, 103, 1837–1850.

Luberda-Durnaś, K., Szczerba, M., Lempart, M., Ciesielska, Z., and Derkowski, A. (2019) Layers stacking disorder in Mg-Fe chlorites based on powder X-ray diffraction data. American Mineralogist, in press.

MacKenzie, K.J.D., and Berezowski, R.M. (1981) Thermal and Mössbauer studies of iron-containing hydrous silicates. I. Cronstedtite. Thermochimica Acta, 44, 171–187.

——— (1984) Thermal and Mössbauer studies of iron-containing hydrous silicates. V.Berthierine. Thermochimica Acta, 74, 291–312.

MacKenzie, K.J.D., Berezowski, R.M., and Bowden, M.E. (1986) Thermal and Mössbauer studies of iron-containing hydrous silicates. VI. Minnesotaite. Thermochimica Acta, 99, 273–289.

Masci, L., Dubacq, B., Verlaguet, A., Chopin, C., De Andrade, V., and Herviou, C. (2019) A XANES and EPMA study of Fe^{3+} in chlorite: Importance of oxychlorite and implications for cation site distribution and thermobarometry. American Mineralogist, 104, 403–417.

Ming, D.W., Jr, P.D.A., Glavin, D.P., Eigenbrode, J.L., Franz, H.B., Sutter, B., Brunner, A.E., Stern, J.C., Freissinet, C., McAdam, A.C., and others (2014) Volatile and organic compositions of sedimentary rocks in Yellowknife. Science, 343, 1–10.

Moore, D.M., and Reynolds, R.C. (1997) X-ray Diffraction and the Identification and Analysis of Clay Minerals, 233–235 p. Oxford University Press, U.K.

Morgan, D.J., Warrington, S.B., and Warne, S.S.J. (1988) Earth sciences applications of evolved gas analysis: A review. Thermochimica Acta, 135, 207–212.

Mustard, J.F., Murchie, S.L., Pelkey, S.M., Ehlmann, B.L., Milliken, R.E., Grant, J.A., Bibring, J.P., Poulet, F., Bishop, J., Dobrea, E.N., and others (2008) Hydrated silicate minerals on Mars observed by the Mars Reconnaissance Orbiter CRISM instrument. Nature, 454, 305–309.

Norman, D.I., and Palin, M. (1982) Volatiles in phyllosillicate minerals. Nature, 551–553.

Prieto, A.C., Lobon, J.M., Alia, J.M., Rull, F., and Martin, F. (1991) Thermal and spectroscopic analysis of natural trioctahedral chlorites. Journal of Thermal Analysis, 37, 969–981.

Rancourt, D.G., Tume, P., and Lalonde, A.E. (1993) Kinetics of the $(Fe^{2+} + OH^{-})_{mica} \rightarrow (Fe^{3+} + O^{2-})_{mica} + H$ oxidation reaction in bulk single-crystal biotite studied by Mössbauer spectroscopy. Physics and Chemistry of Minerals, 20, 267–284.

Rancourt, D.G., Mercier, P.H.J., Cherniak, D.J., Desgreniers, S., Kodama, H., Robert, J.L., and Murad, E. (2001) Mechanisms and crystal chemistry of oxidation in annite: resolving the hydrogen-loss and vacancy reactions. Clays and Clay Minerals, 49, 455–491.

Redfern, S.A.T. (1987) The kinetics of dehydroxylation of kaolinite. Clay Minerals, 22, 447–

456.

Ross, G.J., and Kodama, H. (1974) Experimental transformation of a chlorite into a vermiculite. Clays and Clay Minerals, 22, 205–211.

Rouxhet, P., Gillard, J., and Fripiat, J. (1972) Thermal decomposition of amosite, crocidolite, and biotite. Mineralogical Magazine, 38, 583–592.

Sanz, J., González-Carreño, T., and Gancedo, R. (1983) On dehydroxylation mechanisms of a biotite in vacuo and in oxygen. Physics and Chemistry of Minerals, 9, 14–18.

Schmidt, M.W., and Poli, S. (1998) Experimentally based water budgets for dehydrating slabs and consequences for arc magma generation. Earth and Planetary Science Letters, 163, 361–379.

Shirozu, H. (1980) Cation distribution, sheet thickness, and O-OH space in trioctahedral chlorites- an X ray and infrared study. Mineralogical Journal, 10, 14–34.

——— (1985) Infrared spectra of trioctahedral chlorites in relation to chemical composition. Clay Science, 176, 167–176.

Steudel, A., Kleeberg, R., Koch, C.B., Friedrich, F., and Emmerich, K. (2016) Thermal behavior of chlorites of the clinochlore-chamosite solid solution series: Oxidation of structural iron, hydrogen release and dehydroxylation. Applied Clay Science, 132–133, 626–634.

Taylor, G.L., Ruotsala, a. P., and Keeling, R.O. (1968) Analysis of iron in layer silicates by Mössbauer spectroscopy. Clays and Clay Minerals, 16, 381–391.

Tripathi, R.P., Chandra, U., Chandra, R., and Lokanathan, S. (1978) A Mössbauer study of the effects of heating biotite, phlogopite and vermiculite. Journal of Inorganic and Nuclear Chemistry, 40, 1293–1298.

Truche, L., Joubert, G., Dargent, M., Martz, P., Cathelineau, M., Rigaudier, T., and Quirt, D. (2018) Clay minerals trap hydrogen in the Earth's crust: Evidence from the Cigar Lake uranium deposit, Athabasca. Earth and Planetary Science Letters, 493, 186–197.

Tyrna, P.L., and Guggenheim, S. (1991) The crystal structure of norrishite , $KLiMn_2^{3+}Si_4O_{12}$: An oxygen-rich mica. American Mineralogist, 76, 266–271.

789 Vedder, W., and Wilkins, R. (1969) Dehydroxylation and rehydroxylation, oxidation and
790 reduction of mica. American Mineralogist, 54, 482–509.

791 Villiéras, F., Tvon, J., Cases, J.M., Zimmermann, J.L., and Baeza, R. (1992) Dosage et
792 localisation du fer II dans le talc et la chlorite par analyse apectrometrique des gaz de
793 thermolyse. Comptes Rendus de l'Académie des Sciences Paris, 315, 1201–1206.

794 Walker, J.R., and Bish, D.L. (1992) Application of Rietveld refinement techniques to a
795 disordered *II*b Mg-chamosite. Clays and Clay Minerals, 40, 319–322.

796 Wiewióra, A., and Weiss, Z. (1990) Crystallochemical classifications of phyllosilicates based
797 on the unified system of projection of chemical composition: III. The chlorite group.
798 Clay Minerals, 25, 83–92.

799 Zema, M., Ventruti, G., Lacalamita, M., and Scordari, F. (2010) Kinetics of Fe-
800 oxidation/deprotonation process in Fe-rich phlogopite under isothermal conditions.
801 American Mineralogist, 95, 1458–1466.

802 Zhan, W., and Guggenheim, S. (1995) The dehydroxylation of chlorite and the formation of
803 topotactic product phases. Clays and Clay Minerals, 43, 622–629.

804

This is a preprint, the final version is subject to change, of the American Mineralogist (MSA)
Cite as Authors (Year) Title. American Mineralogist, in press.
DOI: https://doi.org/10.2138/am-2020-7326

Table 1. The samples characterization, indexing, origin, and preparation procedure.

Name	**Sample**[a]	**Stoichiometric formula**[b]	**Location**	**Preparation (Grinding)**	**Reference**
SG7	Chamosite	$[Fe^{2+}_{3.75}Mg_{0.45}Mn_{0.08}\ Al_{1.34}Fe^{3+}_{0.24}\square_{0.14}][(Si_{2.64}Al_{1.36})O_{10}(OH)_8]$	Strzegom, Poland	Mortar[c]	Luberda-Durnaś et al. (2019)
MtBl[2]	Mg-rich chamosite	$[Fe^{2+}_{3.37}Mg_{0.93}Mn_{0.08}\ Al_{1.33}Fe^{3+}_{0.18}\square_{0.11}][(Si_{2.65}Al_{1.35})O_{10}(OH)_8]$	Plan de l'Aguille, Massif du Mont-Blanc, France	Mortar[c]	Lempart et al. (2018)
CCa-2	Fe-rich clinochlore	$[Fe^{2+}_{1.755}Mg_{2.8}Al_{1.22}Fe^{3+}_{0.15}\square_{0.08}][(Si_{2.68}Al_{1.32})O_{10}(OH)_8]$	Flagstaff Hill, El Dorado County, California, USA	McCrone[d]	Luberda-Durnaś et al. (2019)
Sptb[2]	Fe-rich clinochlore	$[Fe^{2+}_{1.33}Mg_{3.35}Mn_{0.01}Al_{1.17}Fe^{3+}_{0.085}\square_{0.055}][(Si_{2.79}Al_{1.21})O_{10}(OH)_8]$	Spitsbergen, Norway	Mortar[c]	Lempart et al. (2018)
Mal	Clinochlore	$[Fe^{2+}_{0.32}Mg_{4.42}Al_{1.105}Fe^{3+}_{0.085}Cr_{0.02}Ni_{0.02}\square_{0.05}][(Si_{2.81}Al_{1.19})O_{10}(OH)_8]$	Malacachetta, Brazil	McCrone[d]	Luberda-Durnaś et al. (2019)

POST	Clinochlore	$[Fe^{2+}_{0.11}Mg_{4.56}Al_{1.27}\ Fe^{3+}_{0.002}\square_{0.06}]\ [(Si_{2.83}Al_{1.17})\ O_{10}(OH)_8]$	Flagstaff Hill, El Dorado County, California, USA	McCrone[c]	Luberda-Durnaś et al. (2019)
LP-6	Biotite	$K_{0.94}[Fe^{2+}_{0.525}Mg_{2.11}Mn_{0.01}Ni_{0.003}Cr_{0.0025}Ti_{0.09}Al_{0.13}Fe^{3+}_{0.12}][(Si_{2.81}Al_{1.19})\ O_{10}(OH_{1.70}F_{0.06})]$	Okanogan Highlands, Washington State, USA	Mortar[e]	Ingamells and Engels (1976)

Notes: [a] – Bayliss' et al. (2005) nomenclature accepted by AIPEA (Guggenheim et al. 2006); [b] – Mineral formulas calculated without assumption that Fe(III) may be a result of dehydrogenation (Masci et al. 2019), based on 14 oxygen atoms; [c] – gently ground with a mortar to pass through a <100 μm sieve; [d] – ground with hexane in a McCrone micronizing mill for 5 minutes; [e] – LP-6's original 40-60 mesh (~389-200 μm) gently ground in a mortar to pass through a <100 μm sieve.

This is a preprint, the final version is subject to change, of the American Mineralogist (MSA)
Cite as Authors (Year) Title. American Mineralogist, in press.
DOI: https://doi.org/10.2138/am-2020-7326

Table 2. Total mass losses, $\Delta m_{dx,}$ generated during 20°C min^{-1} ramp heating coupled with MS data for ion current intensities of H_2^+ and H_2O^+.

Sample	**H_2O(+)**	**Fe(II) (apfu)**	**Fe^{2+}/ (Fe^{2+}+Mg)**	**Δm_{dx} in N_2 (wt%)**	**Δm_{dx} in air (wt%)**	**H_2^+ /H_2O^+ in N_2**	**$H_2^+{}_I$/$H_2^+{}_{II}$ in N_2**	**$H_2O^+{}_I$/$H_2O^+{}_{II}$ in N_2**
SG7	10.57	3.75	0.90	10.16	6.07	0.0019	8.97	7.15
MtBl	10.77	3.37	0.78	10.08	6.65	0.0017	4.13	6.10
CCa-2	11.73	1.755	0.38	10.92	8.98	0.0011	1.60	3.55
Sptb	12.00	1.33	0.28	11.50	10.04	0.0007	1.13	1.82
Mal	12.66	0.32	0.07	12.70	12.31	0.00025	-[c]	3.13
POST	12.91	0.11	0.02	12.81	12.50	<0.0001	-	4.14
LP-6	3.53[a]	1.05[a]	0.20	2.13	1.54	- [b]	-	-

Notes: Δm_{dx} – total mass loss corresponding to complete dehydroxylation up to 1000°C at 20°C/min in N_2; H_2^+ /H_2O^+ **-** ratio of peak areas from m/z = 2 and m/z = 18 signals; I and II subscripts – corresponding the first and second (low- and high-temperature, respectively) peaks in H_2O and H_2 gas profiles tentatively associated with interlayer and 2:1 layer reactions, respectively. H_2O(+) – the maximum theoretical water content due to complete dehydroxylation was calculated based on chemical formula and following Equation 1 (apfu).

This is a preprint, the final version is subject to change, of the American Mineralogist (MSA)
Cite as Authors (Year) Title. American Mineralogist, in press.
DOI: https://doi.org/10.2138/am-2020-7326

[a] – per 6 cations in the octahedral sheet of the 2:1 layer (biotite); [b] – not determined due to the lack of defined H_2O peak in MS profile; [c] – a blurry, broad H_2 peak between 400 °C and 800 °C.

This is a preprint, the final version is subject to change, of the American Mineralogist (MSA)
Cite as Authors (Year) Title. American Mineralogist, in press.
DOI: https://doi.org/10.2138/am-2020-7326

Table 3. Coefficient of determination (R^2) for the linear correlation between the ion current corresponding to H_2O^+ (m/z 18) and the derivative thermogravimetric (DTG) curve determined in relation to the elapsed ramp-heating time for all the studied samples.

Sample	**(DTG/H_2O^+ in N_2) R^2**	**(DTG/H_2O^+ in AIR) R^2**
SG7	0.991	0.603
MtBl	0.984	0.969
CCa-2	0.991	0.985
Sptb	0.991	0.953
Mal	0.993	0.974
POST	0.995	0.997
LP-6	0.922	0.879
SG7 AIR N_2	0.993[a]	0.542[b]

Notes: SG7 AIR N_2 is the SG7 chamosite tested in the experiment shown in Fig. 6. [a] – the second step, after switching gases – ramp heating between 460°C and 1000°C in N_2; [b] – the first step, before switching gases – ramp heating up to 460°C in synthetic air.

This is a preprint, the final version is subject to change, of the American Mineralogist (MSA)
Cite as Authors (Year) Title. American Mineralogist, in press.
DOI: https://doi.org/10.2138/am-2020-7326

Table 4. Fitted Mössbauer parameters for tested chlorites and biotite before (pristine sample) and after ramp heating experiments (to 1000 °C, in N_2 gas or air).

Sample		Fe(II)					Fe(III)				
		IS (mm/s)	QS (mm/s)	FWHM (mm/s)	I (%)	C_f (%)	IS (mm/s)	QS (mm/s)	FWHM (mm/s)	I (%)	C_f (%)
SG7	Unheated	1.11	2.58	0.14	66(3)	-	0.44	0.64	0.22	6(4)	-
		1.12	2.28	0.19	28(4)						
	Heated in N_2	1.17	2.76	0.15	33(1)	66	0.43	0.75	0.25	15(1)	13
		1.18	1.85	0.27	31(3)						
							Fe(II) - (III)[a]				
							0.84	1.58	0.25	21(3)	-
	Heated in air	-	-	-	-	-	0.34	0.42	0.38	100	-
MtBl	Unheated	1.14	2.85	0.13	19(2)	-	0.45	0.56	0.34	5(1)	
		1.14	2.63	0.13	42(3)						
		1.14	2.39	0.25	34(2)						
	Heated in N_2	1.17	2.70	0.17	17(3)	59	0.40	0.88	0.21	14(3)	12
		1.17	2.02	0.25	40(3)						
							Fe(II) - (III)[a]				
							1.04	1.18	0.36	29(3)	-
CCa-2	Unheated	1.13	2.46	0.23	41(6)	-	0.43	0.57	0.37	8(1)	-
		1.125	2.67	0.14	51(7)						
	Heated in N_2	1.16	2.86	0.14	25(3)	71	0.44	0.81	0.31	34(3)	29
		1.09	2.10	0.32	41(5)						
	Heated in air	-	-	-	-	-	0.42	0.47	0.37	100	-

Sptb	**Unheated**	1.13	2.82	0.11	17(2)	-	0.44	0.6	0.33	6(1)	-
		1.14	2.63	0.12	45(3)						
		1.13	2.42	0.24	32(2)						
	Heated in N_2	1.13	2.90	0.14	30(1)	72	0.40	0.85	0.31	33(1)	28
		1.07	2.19	0.29	37(2)						
Mal	**Unheated**	1.13	2.62	0.14	36(5)	-	0.42	0.76	0.47	19(3)	-
		1.13	2.8	0.14	19(3)		0.26	0.65	0.1	2(1)	
		1.11	2.43	0.28	24(2)						
	Heated in N_2	1.08	2.83	0.18	50(3)	75	0.39	0.85	0.33	29(3)	25
		0.98	2.16	0.28	21(2)						
POST	**Unheated**	1.13	2.48	0.28	44(14)	-	0.2	1.1	0.28	2(1)	-
		1.125	2.70	0.19	54(16)						
LP-6	**Unheated**	1.07	2.42	0.13	17(2)	80	0.50	0.63	0.19	15(2)	20
		1.24	2.53	0.15	59(2)		0.63	0.91	0.15	9(2)	
	Heated in N_2	1.28	2.56	0.16	5(1)	6	0.43	1.64	0.31	28(5)	94
							0.28	0.53	0.24	23(2)	
							0.37	1.09	0.29	45(7)	

Notes: IS – isomer shift; QS – electric quadrupole splitting; FWHM - peak width, I – intensity (area) of the total spectrum, C_f –Fe content corrected with respect to the temperature-dependent recoil-free fraction (see Supplemental Information).

[a] component corresponding to "the delocalization of electrons between adjacent Fe^{3+} and Fe^{2+}, resulting in an averaged value of IS that can be assigned to $Fe^{2.5+}$" (Dyar et al. 2006).

Figure captions

Figure 1. TG and DTG curves of tested chlorites combined with H_2O (m/z 18) and H_2 (m/z 2) evolved gas profiles (MS) obtained during ramp heating at a 20 °C/min rate in a nitrogen gas atmosphere (N_2) and in synthetic air (AIR): SG7 (**a**); MtBl (**b**); CCa-2 (**c**); Sptb (**d**); Mal (**e**) POST (**f**). Δm_{dx} – total mass loss corresponding to complete dehydroxylation up to 1000°C.

Figure 2. Theoretical H_2O content calculated following Equation 1, $H_2O(+)$, and total mass losses obtained experimentally during heating at a 20°C/min rate (Δm_{dx}) in nitrogen and synthetic air gas up to 1000 °C, and the H_2^+/H_2O^+ ratio obtained from simultaneous evolved gas analysis, plotted as a function of Fe(II) content in six tested chlorites. The shaded region indicates the difference between Δm_{dx} obtained in nitrogen and synthetic air gas.

Figure 3. LP-6 biotite TG and DTG curves (**a, c**) combined with H_2O and H_2 evolved gas profiles (**b, d**) obtained during ramp heating at a 20 °C/min rate in a nitrogen gas atmosphere (**N_2**; **a, b**) and in synthetic air (**AIR**; **c, d**).

Figure 4. TG and DTG curves combined with H_2O and H_2 evolved gas profiles obtained under an N_2 atmosphere during isothermal heating of MtBl at 400 °C for 48h followed by ramp heating at a 20°C/min rate.

Figure 5. SG7 (**a, b**) and POST (**c, d**) as end-member chlorites represented two extreme cases when heated under synthetic air (*cf.* Figs. 1a, e) showing poor and strong linear relationships between the DTG curve and H_2O^+ mass spectrum (in the ion current corresponding to m/z 18), respectively; R^2 - the coefficient of determination for linear correlation.

Figure 6. SG7 sample ramp heated at a 20°C/min rate in synthetic air gas up to temperature of 460°C, followed by switching the purge gas to nitrogen to continue ramp heating up to

1000°C. TG and DTG curves (**a**), evolved gas profiles of H_2 and H_2O (**b**), a dotted line shows the temperature point of gas switching.

Figure 7. OH stretching region of thermo-DRIFT spectra of chamosite (SG7) (**a, b**) and Fe-clinochlore (Sptb) (**c, d)** heated *in situ* up to predefined temperatures in nitrogen gas (N_2) and in synthetic air (AIR), respectively.

Supplemental Figure captions

Supplemental Figure S1. Mössbauer spectra of chlorites (SG7, MtBl, CCa-2, Sptb, Mal) and biotite (LP-6) before and after ramp heating to 1000 °C at a 20 °C/min rate under N_2; measured at 300 K.

Supplementary Figure S2. XRD patterns of heating products of chlorites (1000 °C) (**a**) and biotite (1050 °C) (**b**) obtained under nitrogen gas atmosphere. Fo - forsterite, Fy - fayalite, Sp - spinel-like phase, * - silica XRD spike.

This is a preprint, the final version is subject to change, of the American Mineralogist (MSA)
Cite as Authors (Year) Title. American Mineralogist, in press.
DOI: https://doi.org/10.2138/am-2020-7326

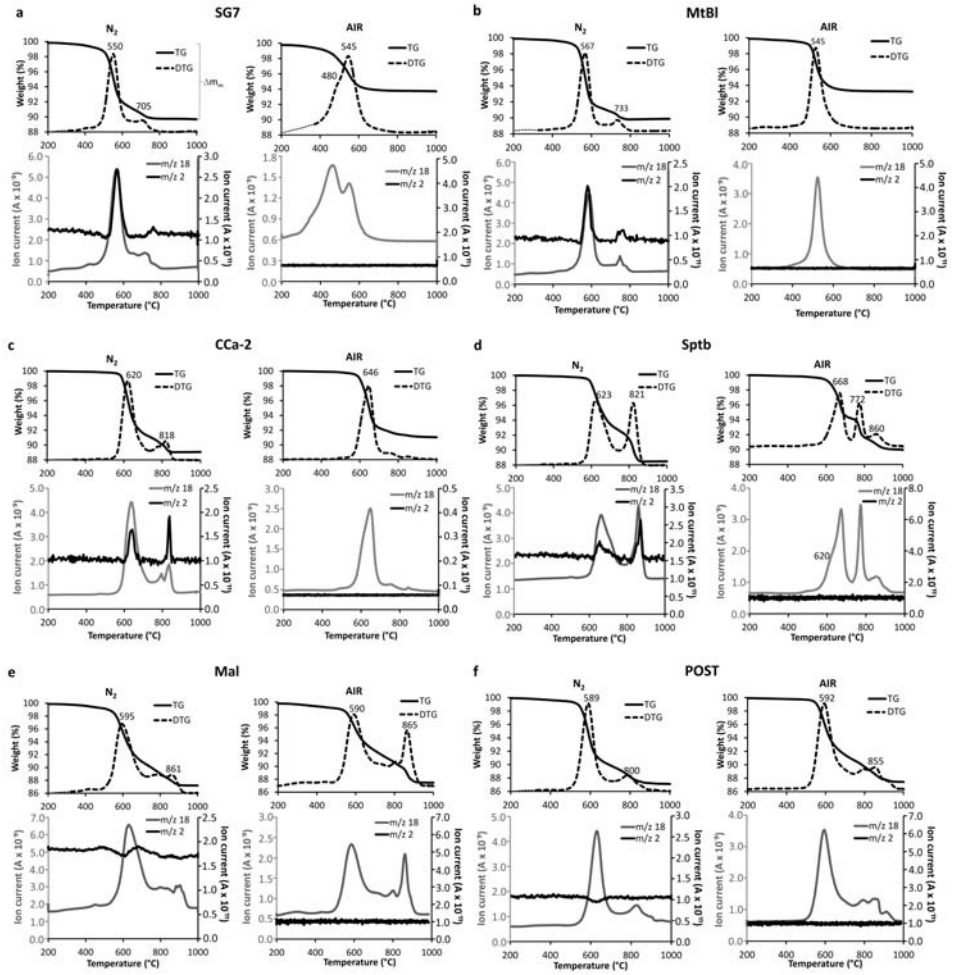

Figure 1

This is a preprint, the final version is subject to change, of the American Mineralogist (MSA)
Cite as Authors (Year) Title. American Mineralogist, in press.
DOI: https://doi.org/10.2138/am-2020-7326

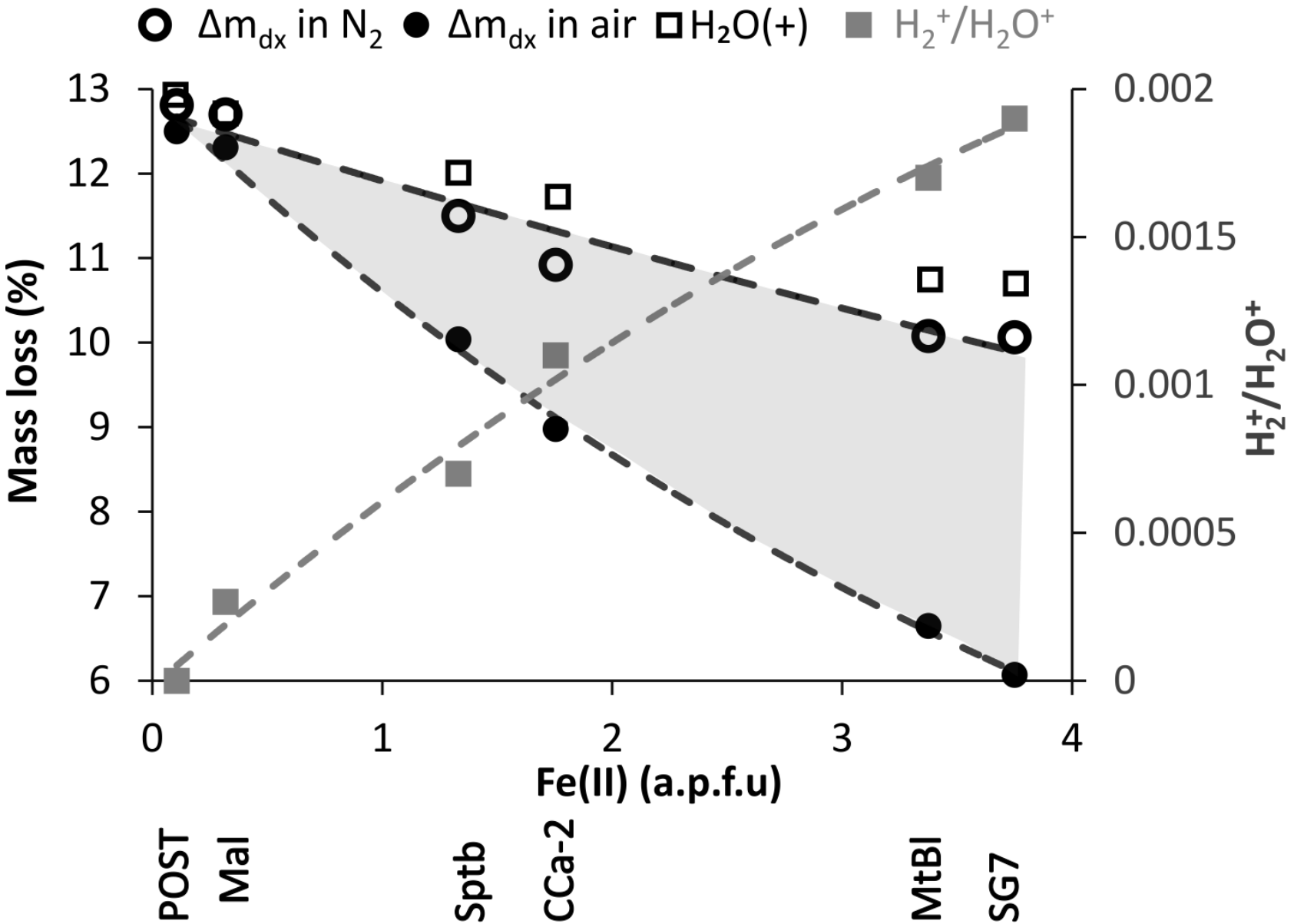

Figure 2

This is a preprint, the final version is subject to change, of the American Mineralogist (MSA)
Cite as Authors (Year) Title. American Mineralogist, in press.
DOI: https://doi.org/10.2138/am-2020-7326

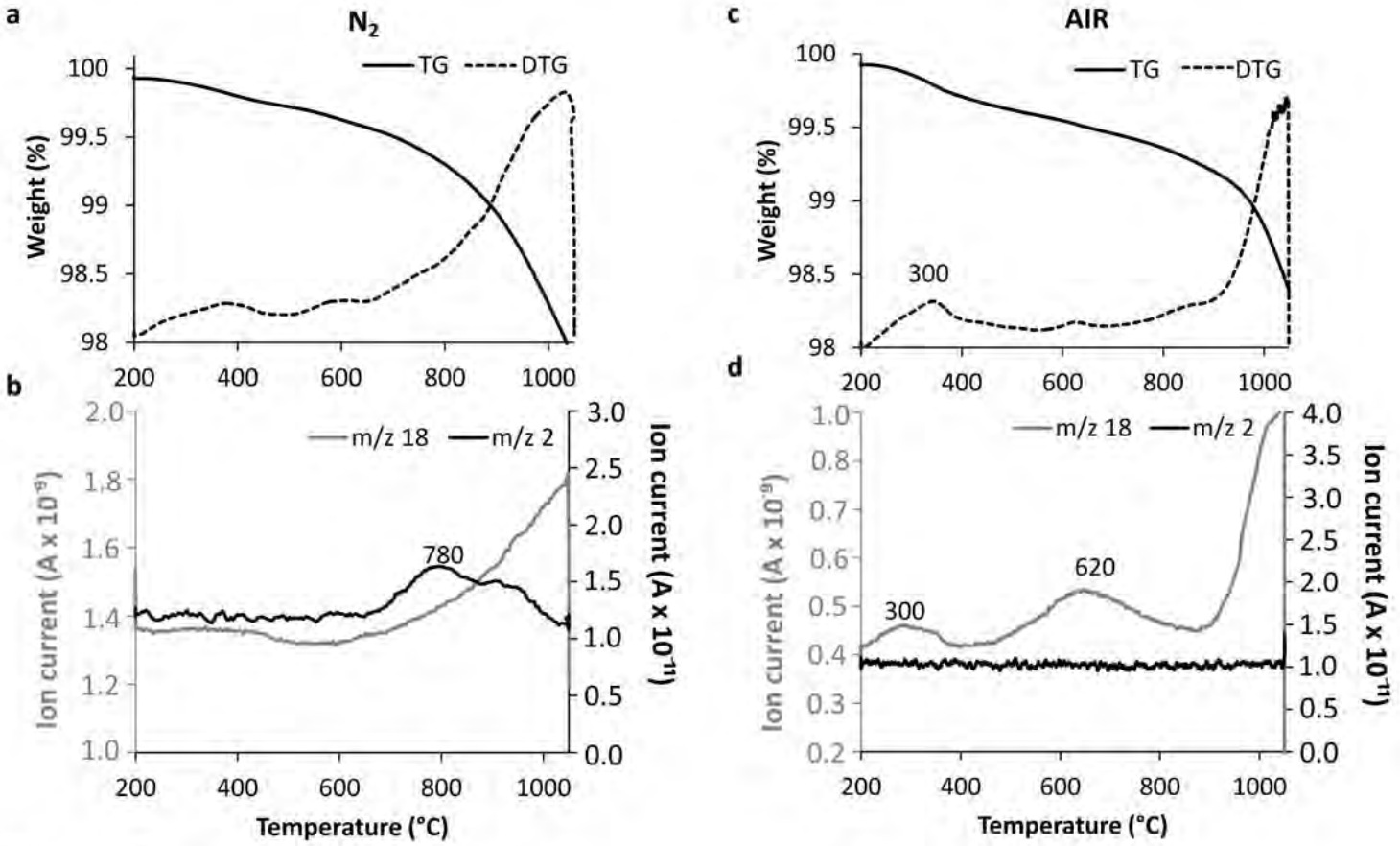

Figure 3

This is a preprint, the final version is subject to change, of the American Mineralogist (MSA)
Cite as Authors (Year) Title. American Mineralogist, in press.
DOI: https://doi.org/10.2138/am-2020-7326

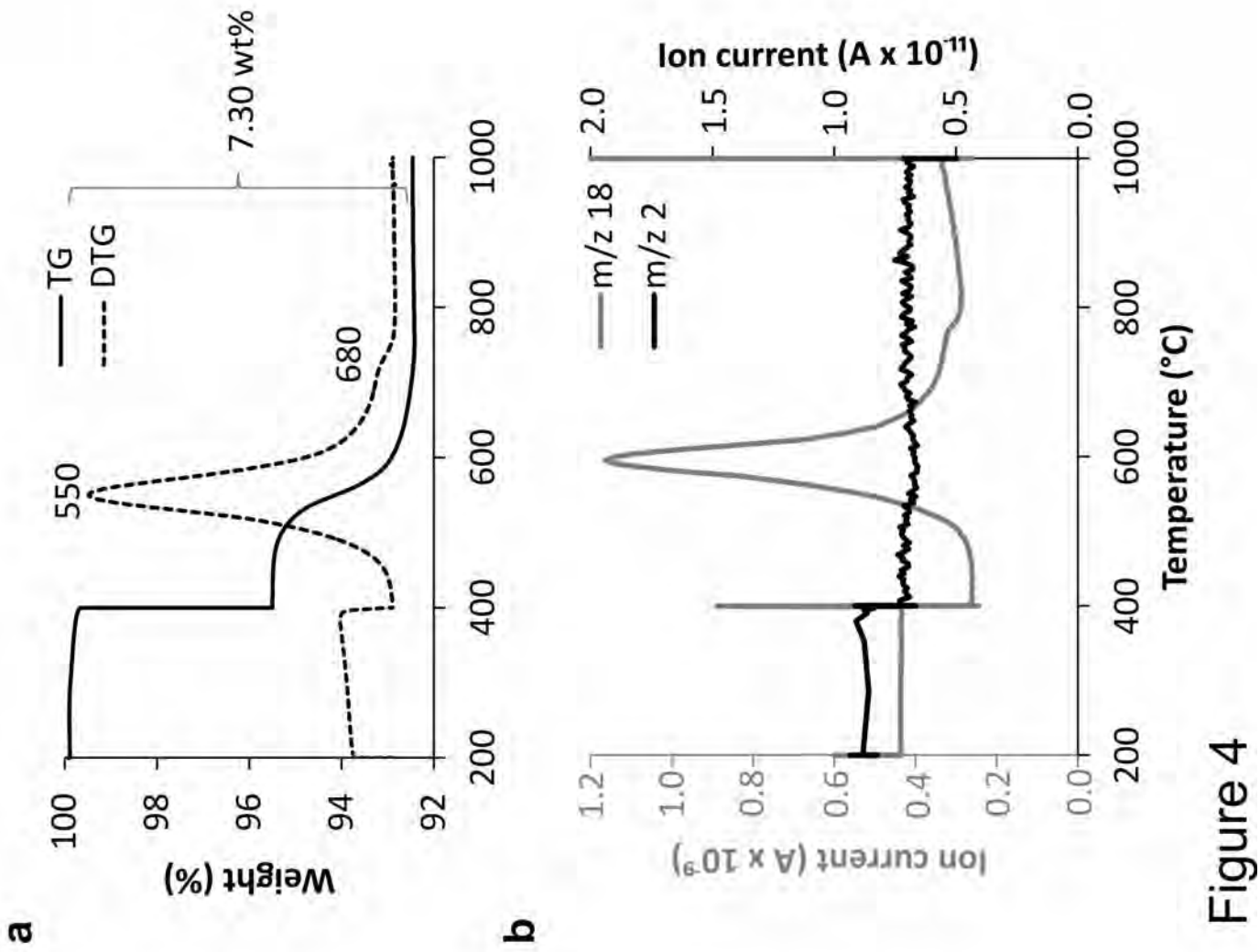

Figure 4

This is a preprint, the final version is subject to change, of the American Mineralogist (MSA)
Cite as Authors (Year) Title. American Mineralogist, in press.
DOI: https://doi.org/10.2138/am-2020-7326

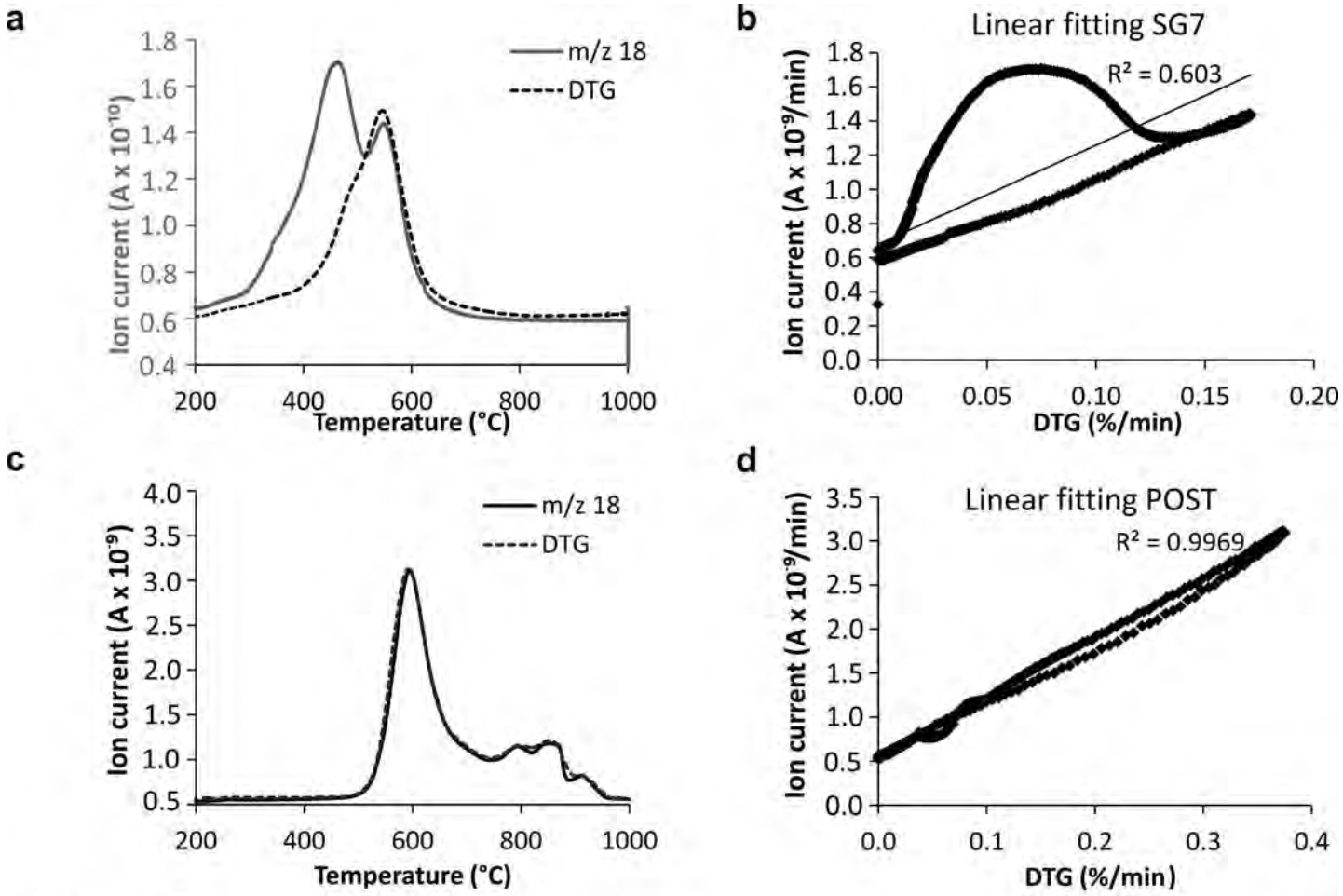

Figure 5

This is a preprint, the final version is subject to change, of the American Mineralogist (MSA)
Cite as Authors (Year) Title. American Mineralogist, in press.
DOI: https://doi.org/10.2138/am-2020-7326

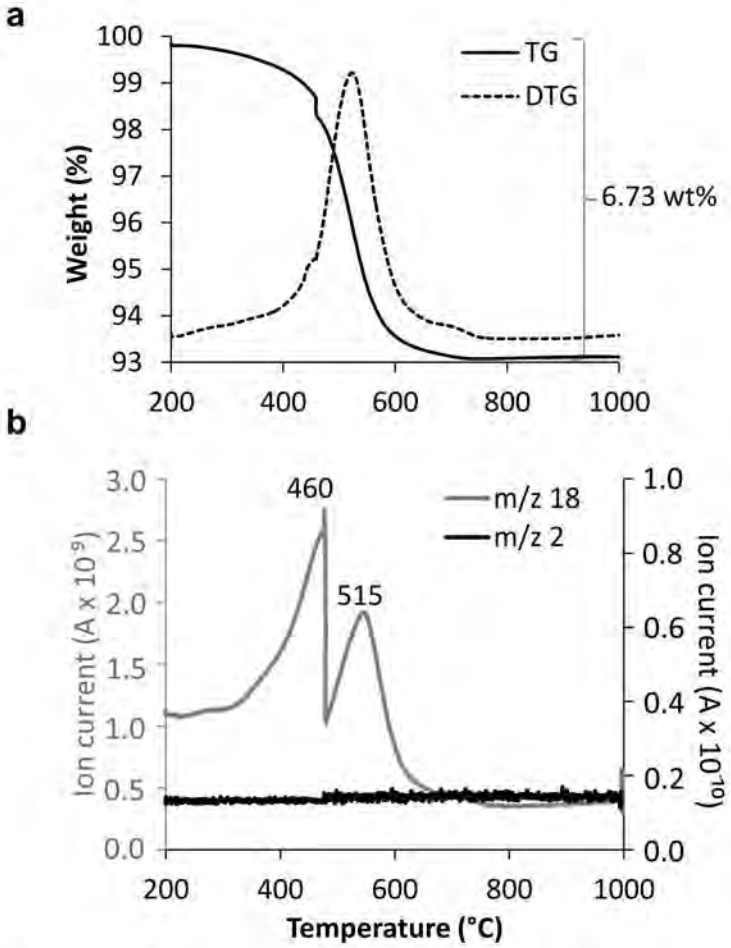

Figure 6

This is a preprint, the final version is subject to change, of the American Mineralogist (MSA)
Cite as Authors (Year) Title. American Mineralogist, in press.
DOI: https://doi.org/10.2138/am-2020-7326

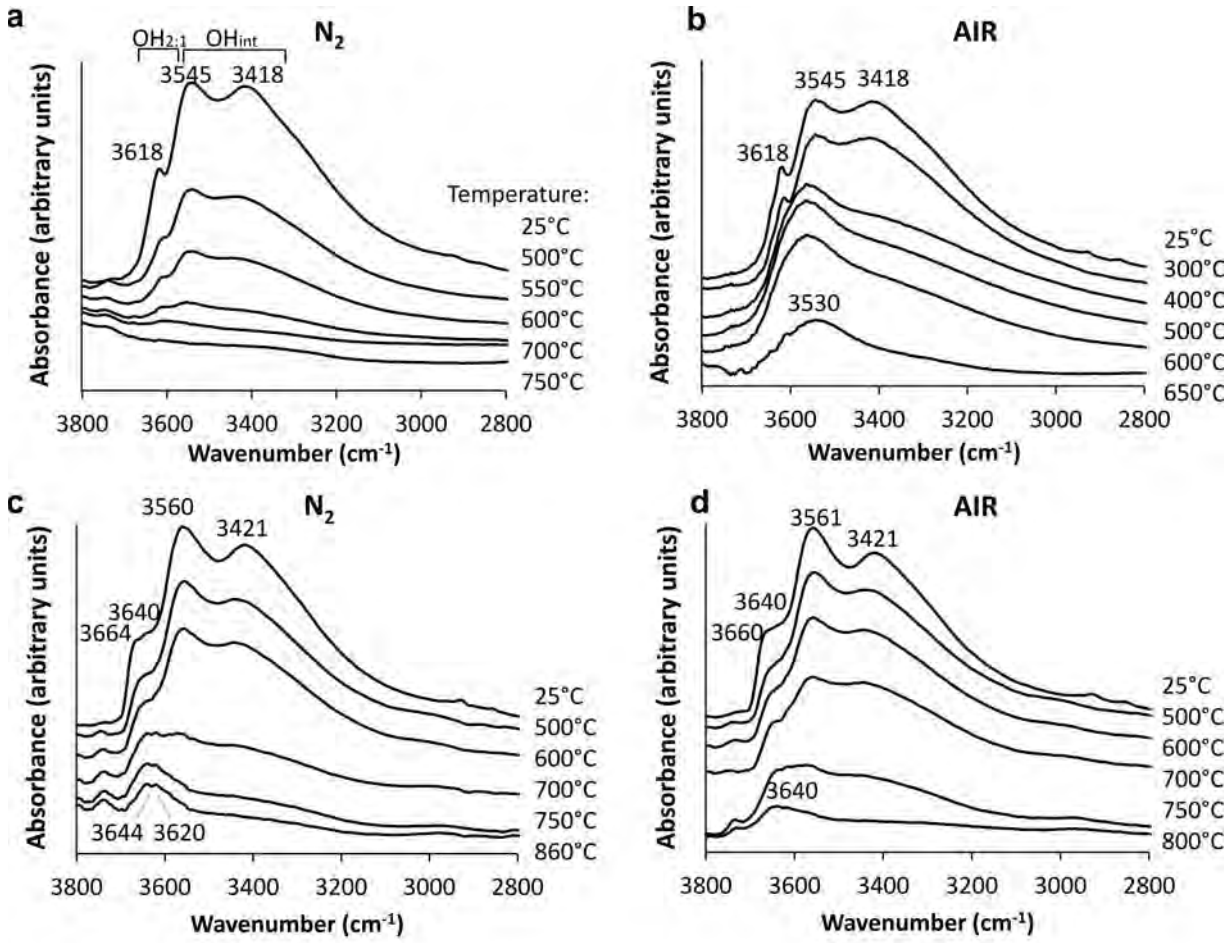

Figure 7